Synchronous multi-segmental activity between metachronal waves controls locomotion speed in *Drosophila* larvae

Yingtao Liu[a,b], Eri Hasegawa[b,e], Akinao Nose[a,b] , Maarten F. Zwart[c*], Hiroshi Kohsaka[b,d*]

[a] Department of Physics, Graduate School of Science, the University of Tokyo, 7-3-1 Hongo, Bunkyo-ku, 133-0033 Tokyo, Japan

[b] Department of Complexity Science and Engineering, Graduate School of Frontier Science, the University of Tokyo, 5-1-5 Kashiwanoha, Kashiwa, 277-8561 Chiba, Japan

[c] School of Psychology and Neuroscience, Centre of Biophotonics, University of St Andrews, St Andrews KY16 9JP, UK

[d] Graduate School of Informatics and Engineering, the University of Electro-Communications, 1-5-1, Chofugaoka, Chofu-shi, 182-8585 Tokyo, Japan

[e] Present address: Frontier Science and Social Co-creation Initiative, Kanazawa University, Kakuma, Kanazawa, 920-1192, Ishikawa, Japan

* For correspondence: mfz@st-andrews.ac.uk; kohsaka@edu.k.u-tokyo.ac.jp; +81-42-443-5528

Abstract

The ability to adjust the speed of locomotion is essential for survival. In limbed animals, the frequency of locomotion is modulated primarily by changing the duration of the stance phase. The underlying neural mechanisms of this selective modulation remain an open question. Here, we report a neural circuit controlling a similarly selective adjustment of locomotion frequency in *Drosophila* larvae. *Drosophila* larvae crawl using peristaltic waves of muscle contractions. We find that larvae adjust the frequency of locomotion mostly by varying the time between consecutive contraction waves, reminiscent of limbed locomotion. A specific set of muscles, the lateral transverse (LT) muscles, co-contract in all segments during this phase, the duration of which sets the duration of the interwave phase. We identify two types of GABAergic interneurons in the LT neural network, premotor neuron A26f and its presynaptic partner A31c, which exhibit segmentally synchronized activity and control locomotor frequency by setting the amplitude and duration of LT muscle contractions. Altogether, our results reveal an inhibitory central circuit that sets the frequency of locomotion by controlling the duration of the period in between peristaltic waves. Further analysis of the descending inputs onto this circuit will help understand the higher control of this selective modulation.

Introduction

Animals flexibly adapt their speed of locomotion to meet their behavioral needs (Alexander, 1989; Byrne, 2019; DeAngelis et al., 2019). In recent decades, the neural basis of the modulation of the speed of locomotion across the animal kingdom has received much attention. The mesencephalic locomotor region (MLR), which projects to reticulospinal neurons that in turn innervate spinal circuits, has been identified in all vertebrate species studied to date as an important control centre (Ryczko et al., 2017). Increasingly intense stimulation of the MLR causes increases in the speed of locomotion, with accompanying gait transitions (Atsuta et al., 1990; Grillner, 1985; Shik et al., 1966; Shik and Orlovsky, 1976;

Skinner and Garcia-Rill, 1984). The spinal cord recruits different types of motor neurons at different speeds, with the accompanying changes in gait requiring widespread reconfiguration within its circuitry (Dasen, 2017; Kiehn, 2016).

How does the central nervous system vary the frequency of locomotion to achieve the required speeds? In a range of species, descending projecting excitatory neurons have been shown to drive the rhythm of locomotion (Berg et al., 2018; Caggiano et al., 2018; Capelli et al., 2017; Friesen and Kristan, 2007; Gatto and Goulding, 2018; Josset et al., 2018; Roberts et al., 2010). In mice, studies using optogenetics have shown that excitatory neurons are necessary and sufficient for rhythm generation (Hägglund et al., 2010, 2013), with studies ongoing to uncover the precise identity of the rhythm generators (Kiehn, 2016). Zebrafish, which use axial locomotion to move, have different central modules corresponding in adults to fast, intermediate, and slow locomotion that are selectively recruited to command the motor pools specific for different speeds (Ampatzis et al., 2013, 2014). The pacemaker neurons driving locomotion at different speeds have intrinsic bursting frequencies related to their module affiliation (Song et al., 2020).

The kinematics of movement change as a function of frequency depending on the species and gait. Swimming animals modulate their undulatory frequency by controlling the intersegmental lag, which is linearly scaled with the locomotor cycle duration (Grillner, 1974). On the other hand, limbed animals change the frequency of walking by varying the locomotor cycle differentially: the stance phase is varied, but the swing phase is almost unchanged, even as animals switch to different gaits. This holds true for animals ranging from insects and tardigrades to mammals (Boije and Kullander, 2018; Frigon et al., 2014; Grillner et al., 1979; Jacobson and Hollyday, 1982; Nirody et al., 2021). How the nervous system generates this asymmetry in the variation of stance and swing phases is still an open question (Bidaye et al., 2018; Boije and Kullander, 2018; Kiehn, 2016).

Here, we investigated the speed-dependent modulation of locomotion in *Drosophila* larvae and the underlying neural mechanisms. The *Drosophila* larva moves by peristaltic

waves, in which body wall muscles contract sequentially from one end to the other (Berrigan and Pepin, 1995; Heckscher et al., 2012; Sun et al., 2022). We found that the *Drosophila* larval locomotor cycle is also differentially modulated: the phase in between each consecutive peristaltic wave (the "interwave" phase), not the peristaltic wave itself, is primarily varied with speed, reminiscent of the stance phase in limbed locomotion. We then examined the underlying muscular dynamics and found that the interwave phase is characterized by synchronous contractions of the lateral transverse (LT) muscles along the anterior-posterior axis. The amplitude and duration of their contraction scale with the duration of the interwave phase. Using EM connectomics and calcium imaging, we identified two types of interneurons that are associated with the LT neural circuitry and show segmentally synchronized activity: GABAergic premotor neuron A26f and its presynaptic partner GABAergic interneuron A31c. Using optogenetics, we revealed that both A31c and A26f neurons are sufficient and necessary for the desired contraction of the LT muscles and set the speed of locomotion through the modulation of the interwave phase. Our results reveal that the *Drosophila* larva uses a similar strategy to regulate speed as limbed animals by varying the two main phases of the cycle differentially and that the activity of an inhibitory circuit generates this variation.

Results

Variability in the interwave phase of crawling contributes to speed variability

Crawling behavior in *Drosophila* larvae is generated by repetitive waves of propagation along the length of their body (Berrigan and Pepin, 1995). A previous study in mildly physically restrained first-instar larvae showed that crawling speed correlates with stride period more than stride length (Heckscher et al., 2012). It has been shown that the lag between the contraction of adjacent segments during the peristaltic wave (intersegmental lag) scales with the cycle period in the intact animal and the isolated central nervous system

(CNS) (Heckscher et al., 2012; Pulver et al., 2015). These observations suggest that the cycle period varies through a uniform, rather than an asymmetric, modulation of the phases of the locomotor cycle. However, these physically restricted larvae have long cycle periods (2-20 seconds), presumably due to aberrant or absent input from sensory neurons (Caldwell et al., 2003; Hughes and Thomas, 2007; Schützler et al., 2019; Zarin et al., 2019). How the larva varies locomotion in free crawling within the normal range of cycle periods (0.6-2 seconds) is therefore not understood. We therefore first aimed to confirm these findings in freely crawling third-instar larvae (Figure 1A-I, Figure 1-supplement A-F). We recorded larvae freely crawling on an agarose plate and measured the displacement of their body-wall segments (Figure 1A-C). Larvae crawled at varying speeds even within the same environmental conditions such as temperature (Figure 1D and 1E, 0.35 – 1.23 mm/sec, n = 18 larvae). We found that the locomotion speed in these freely crawling animals also correlated with stride frequency more so than stride length, consistent with the previous report (Figure 1E). To further characterize the underlying kinematic changes, we assessed how the two previously identified phases within the locomotor cycle (Heckscher et al., 2012) change with speed. In the first phase, local body wall contractions are propagated from the posterior to anterior segments (here called 'wave phase'), whereas the second is characterized by the period from mouth parts unhooking to the onset of the tail contraction ('interwave phase'; Figure 1F).

To examine the possible contribution of the variability in the interwave phase to the speed variability, we analyzed the correlation between crawling speed and the two phases (Figure 1G-I). We found that both the interwave phase and the wave phase are correlated with the speed (Figure 1-supplement C and C'; Pearson correlation coefficient: the wave phase vs speed r = -0.62, the interwave phase vs speed r = -0.74). The interwave duration at faster speed is close to 0. Indeed, the duty factor of the interwave phase, which is given by the ratio of the interwave phase duration to stride duration, decreased with speed (Figure 1I; linear regression coefficient = -0.47, r^2 = 0.55) and was reduced to zero at the faster

129 speeds. The wave and interwave phases are modulated independently, as can be seen by
130 the lack in correlation between these two phases (Figure 1-supplement D and E). These
131 results suggest that the speed-dependent modulation of crawling frequency is largely due to
132 modulation of the interwave phase.

133 We quantified the duration of each phase in freely crawling larvae. To evaluate the
134 contribution of these two phases to stride duration, we plotted the duration of these phases
135 as a function of stride duration (Figure 1-supplement F and F'). Both are correlated with stride
136 duration, with the interwave phase correlated more strongly than the wave phase (interwave
137 phase $r = 0.86$, wave phase $r = 0.56$, $p < 0.0001$). What becomes clear from this analysis is
138 that when stride duration is less than approximately 1 second, the interwave phase is minimal,
139 and the wave duration therefore reduces in duration in line with stride duration; on the other
140 hand, when stride duration is greater than approximately 1.2 seconds, wave duration is more
141 or less constant, with increases in stride duration accompanied by increases in interwave
142 duration. These observations suggest that the interwave phase between peristaltic waves is
143 more variable than wave phase, and that there is a range-dependent modulation of the
144 frequency of locomotion.
145

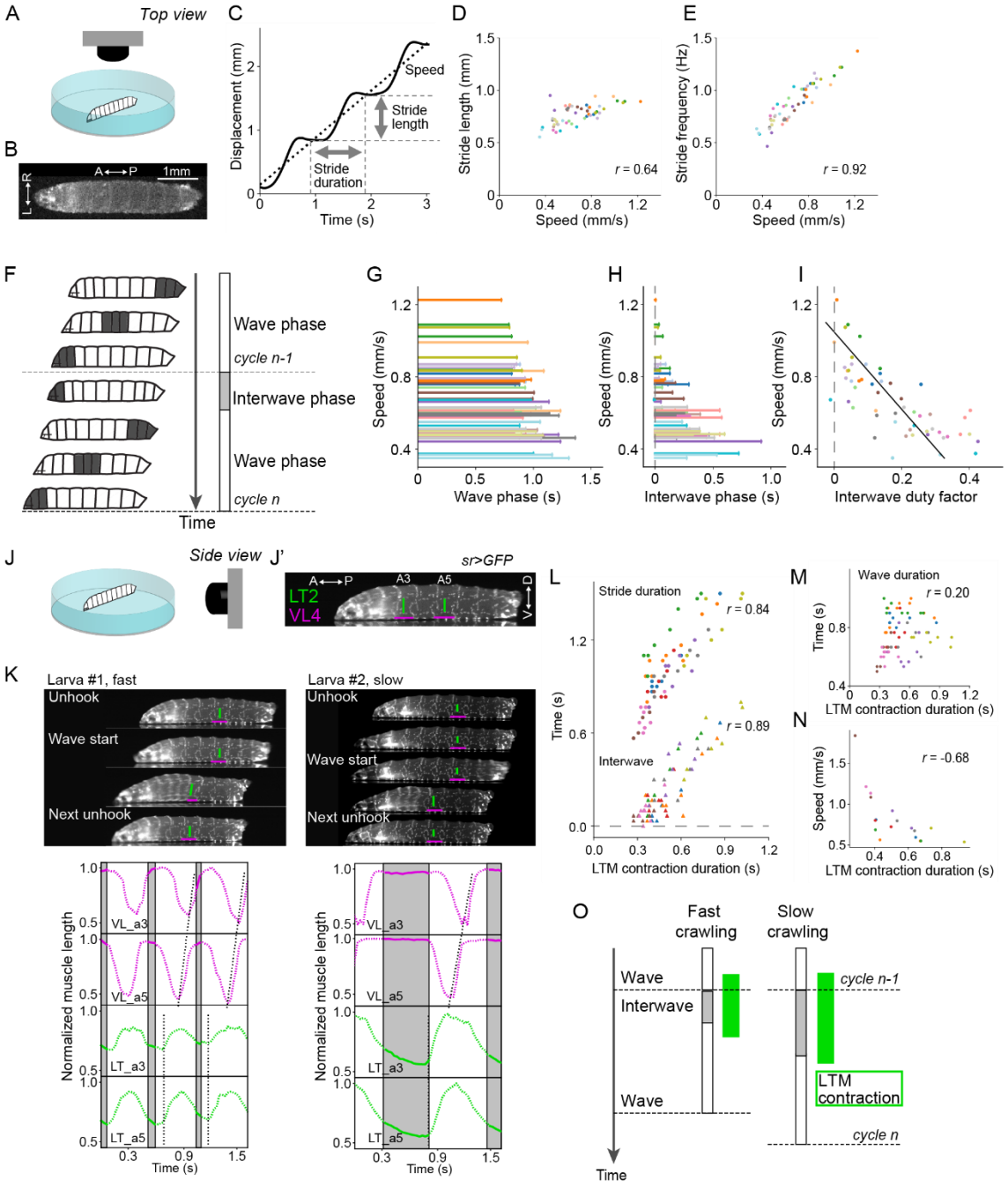

Figure 1. Crawling speed depends on the duration of interwave phase, during which the LT muscles are contracted

(A-I) Recording of locomotion parameters from top view (n = 268 strides, 54 episodes, 18 larvae). **(A)** Schematic drawing of the crawling assay from top view. **(B)** An example frame of top-view recording. **(C)** Measurement of the stride duration, stride length, and speed. **(D)** Relationship between speed and stride length. *r* represents Pearson correlation coefficient. **(E)**

Relationship between speed and stride frequency. **(F)** Schematic representation of the two phases of a locomotor cycle. **(G)** Relationship between the duration of wave phase and speed. **(H)** Relationship between the duration of interwave phase and speed. **(I)** Interwave duty factor, the proportion of interwave phase in the stride duration, decreases with speeds. Linear regression coefficient is -0.47. **(J-O)** Recording of locomotion parameters and muscular kinematics from side view (n = 8 larvae). **(J)** Schematic drawing of the crawling assay from side view. **(J')** An example frame of side-view recording. LT2: lateral transverse muscle 2. VL4: ventral longitudinal muscle 4. **(K)** Representative tracking of the muscle movement during forward crawling. Top left panel shows the muscle movement with a fast speed. Top right panel shows the muscle movement with a slow speed. Bottom panels demonstrate the dynamics of muscle lengths in the data shown in the top panels. **(L)** Relationship between the contraction duration of LT2 muscle and two temporal parameters (stride duration and interwave duration) (Pearson correlation coefficients; stride duration: 0.84 and interwave duration: 0.89). **(M)** Relationship between the contraction duration of LT2 muscle and wave duration (Pearson correlation coefficient: 0.20). **(N)** Relationship between LT2 muscle contraction duration and speed. **(O)** Schematic of the relationship between LT muscle (LTM) contraction and crawling speed. The duration of the two phases and the contraction of LT muscles are correlated with crawling speed.

Synchronous contraction of transverse muscles is correlated with the intervwave phase

To reveal the nature of the interwave phase, we examined the movement of body wall muscles during free crawling. The ends of individual muscles were labelled by expressing GFP in the tendon cells using *sr-Gal4* (Schnorrer et al., 2007) and imaged from the side (Figure 1J and 1J'). This allowed us to analyze the contraction dynamics of each muscle in freely crawling larvae. The dynamics of two longitudinal muscles (DO1 and VL4) that span the anterior and posterior boundary of each segment and one transverse muscle (LT2) that runs perpendicular to the anterior-posterior axis of the animal were examined

(Figure 1K and Figure 1-supplement G). Consistent with the previous study, longitudinal muscles exhibited propagation from the posterior segment to the anterior in forward crawling (Figure 1L and Figure 1-supplement G'). Interestingly, transverse muscles only showed synchronous contractions (Figure 1K and Figure 1-supplement G'). Furthermore, while longitudinal muscles were mostly contracting during peristaltic waves, the transverse muscles contracted during the interwave phase (Figure 1-supplement G').

The phase-specific contraction of transverse muscles implies the possible involvement of transverse muscles during the interwave phase. Accordingly, we analyzed the contraction duration of transverse muscles and analyzed its relationship with the duration of the phases. While the duration of wave phase didn't have a strong correlation, the duration of the interwave phase had a high correlation with the contraction duration of transverse muscles (wave phase $r = 0.20$, interwave phase $r = 0.89$, $p < 0.0001$, Figure 1L and 1M). Stride duration, which is the sum of the wave duration and the interwave duration, also had a strong correlation with the contraction duration of transverse muscles ($r = 0.84$, Figure 1L). This result implies that the contraction duration of transverse muscles should be related to the crawling speed. We therefore plotted the duration of transverse muscle contractions against crawling speed (Figure 1N) and found that they were correlated ($r = -0.68$). Next, we analyzed the relationship between the amplitude of transverse muscle contraction and the crawling kinematics. As is the case of the contraction duration, the contraction amplitude is also correlated with the interphase duration and stride duration but not the wave duration (Figure 1-supplement H-I). On the other hand, the contraction amplitude is weakly correlated with speed (Figure 1-supplement J). These results show that the duration and amplitude of synchronous contraction of transverse muscles are related to the duration of interwave phase (Figure 1O). Importantly, the duration of the synchronous contraction is correlated with crawling speed (Figure 1O).

Identification of GABAergic interneurons A31c showing segmentally synchronized

activity

In a screen for the neurons that are activated during the interwave phase, we identified cell type A31c (Figure 2-supplement). By reviewing the existing genetic driver expression patterns (Li et al., 2014), we identified several genetic drivers targeting the A31c neuron, including a split GAL4 driver (*A31c-a8-sp*) specifically targeting the A31c neuron in segment A8, a split GAL4 driver (*A31c-sp*) targeting A31c neurons in neuromeres A2-A8, and a LexA driver (*A31c-LexA*) that targets A31c neurons in neuromeres A2-A8 with variable expression patterns. We first used these lines to investigate the morphology and neurotransmitter identity of A31c neurons. The neurites project dorsally approximately one neuromere mostly to the anterior (Figure 2A). The synaptic input sites are located along the dorsolateral (DL) tract (Landgraf et al., 2003), while the synaptic output sites are mainly positioned dorsally near the midline (Figure 2A and 2B). Using immunohistochemistry, we found that A31c neurons are GABAergic (Figure 2-supplement A).

We then used a dual-color imaging system to monitor the activity of A31c neurons using *A31c-sp>UAS-CD4::GCAMP6f* and the pan-neuronal activity using *nSyb-LexA>LexAop-RGECO1* in the isolated CNS (Figure 2C-E and Figure 2-supplement B-C; Materials and methods for details). The pan-neuronal activity patterns were used as an indicator of the fictive behaviors produced (Pulver et al., 2015), showing stereotyped fictive forward waves (FW). At the initiation of forward locomotion, all abdominal A31c neurons show burst-like coactivation preceding the forward wave (Figure 2C and 2D). During the FW that follows, A31c neurons in anterior segments A2-A5 are re-activated in a wave-like sequence (Figure 2C and 2D). The intersegmental lags of pan-neuronal activity between neighboring segments show non-zero values which reflects the propagation of neuronal activity along the body axis (Figure 2E). On the other hand, the intersegmental lags of A31c neurons are almost zero consistent with their synchronized activity (Figure 2E). To sum, these results show that A31c neurons exhibit synchronous multi-segmental activity during the interwave phase.

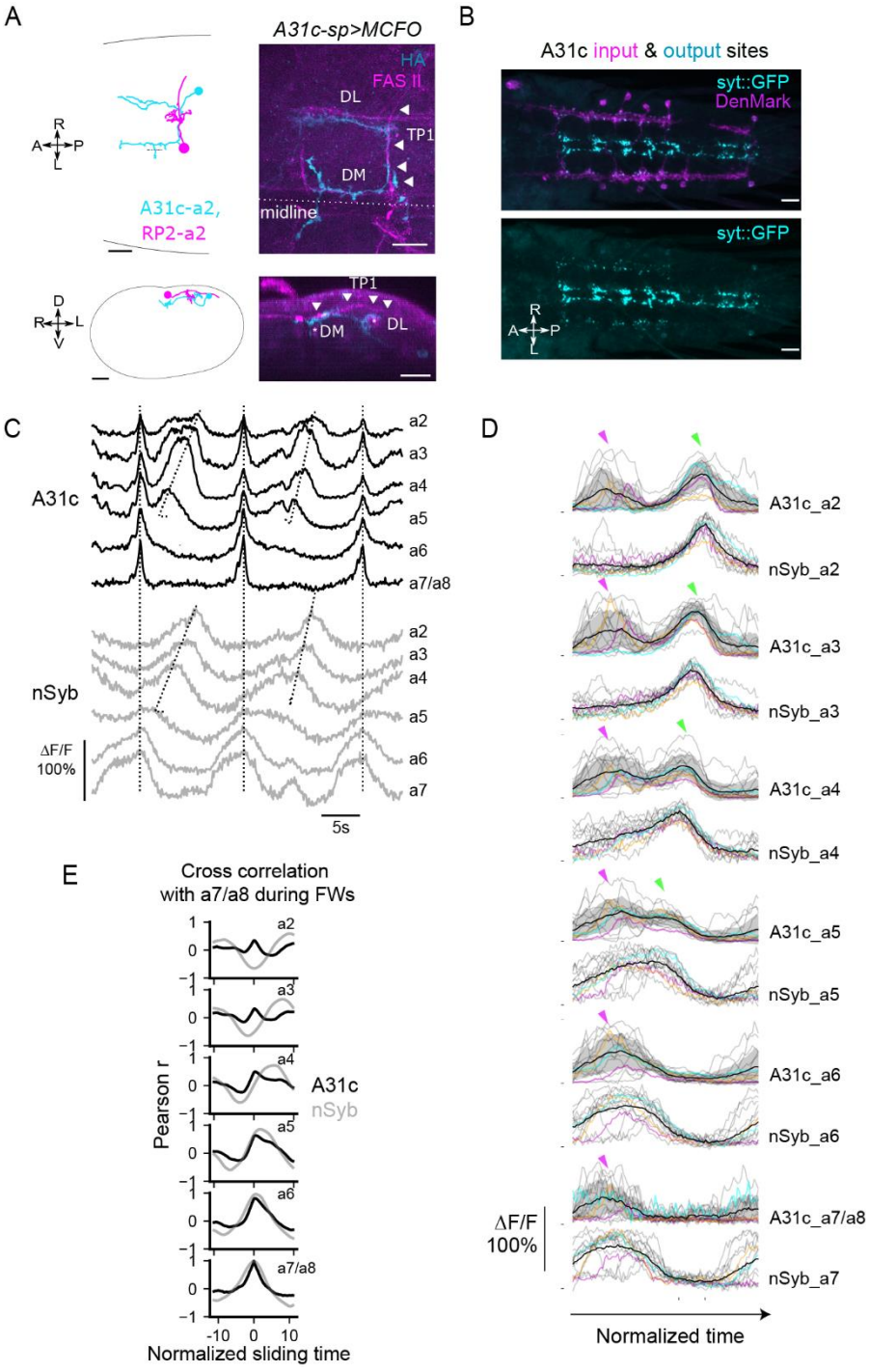

Figure 2. A31c neurons show synchronous activity preceding the forward wave

(A) A31c single-neuron morphology shown by EM reconstruction and genetically mosaic analysis. Scale bars: 20 μm. **(B)** Pre- and post-synapse markers label the input and output sites of A31c neurons (*A31c-sp>UAS-syt::GFP, UAS-DenMark*). Scale bars: 20 μm. **(C-E)** Recording of calcium activity of A31c neurons (*A31c-sp>UAS-CD4::GCaMP6f*) and group activity of nSyb

neurons (*nSyb-LexA>LexAop-RGECO1*) which reports the pan-neuronal activity in fictive locomotion (n = 15 traces, 5 larvae). **(C)** Example recordings of A31c neurons and nSyb neurons in fictive forward locomotion. **(D)** Group data of calcium imaging of A31c neurons and nSyb neurons. Each trace is aligned by activity peak of nSyb_a4 and nSyb_a2 and normalized to 0-1 by the activity maximum and minimum of the whole recording. Magenta arrows indicate the co-activation of A31c neurons. Green arrows indicate the wave-like activity of A31c neurons. Black lines represent the average calcium activity. Shading represents the standard error. Colored lines represent the three example traces. Grey lines represent all other traces. Ticks along the horizontal axis indicate the activity peaks of nSyb_a4 and nSyb_a2. Ticks along the vertical axis indicate the 0. **(E)** Cross correlation of neuronal activity between the neuron in each segment (from A2 to A7/A8) and the one in A7/A8 (black: A31c neurons, grey: nSyb neurons). See Materials and methods for details.

A31c neurons receive synaptic inputs from descending neurons and give synaptic output to local and ascending neurons

To understand the details of the connectivity of this circuit, we reconstructed the connectivity of A31c using EM connectomics (Materials and methods for details). We identified A31c neurons in neuromeres A2-A8 in the database of the larval central nervous system, reconstructed all pre- and post-synaptic partners, and analyzed their connectivity (Figure 3A-3C and Figure 3-supplement A and B). We analyzed the connectivity of A31c neurons in anterior segments A2-A3 and posterior segments A7-A8 separately (Figure 3B-3D). We found that the synaptic inputs to A31c neurons are similar in the anterior and posterior segments, with several descending cell types innervating A31c across segments (Figure 3D). The same suboesophageal (SEG) descending neuron cell type (here labelled “S10”) provides a significant plurality of the synaptic input. Among postsynaptic targets, we found that just one cell type is consistent between segments A2-A3 and A7-A8: A26f neurons, which are among their top three postsynaptic partners (Figure 3D). A26f neurons also receive synaptic inputs from the ascending cell type A19f, one of the top postsynaptic partners of

A31c neurons (Jonaitis, 2020). Interestingly, it has previously been reported that A26f strongly innervates the transverse motor neurons (Zarin et al., 2019; Zwart et al., 2016).

We next used *trans*-Tango, a genetic tool for tracing postsynaptic partners (Talay et al., 2017), to confirm the identity of the postsynaptic neurons of A31c-a8. We repeatedly identified Tango expression in an A26f-like cell type in segment A7, in addition to other neurons, some of which we could identify (four samples showing A26f-a7 neurons; Figure 3-supplement C and D). These results collectively show that A26f neurons are postsynaptic to A31c neurons.

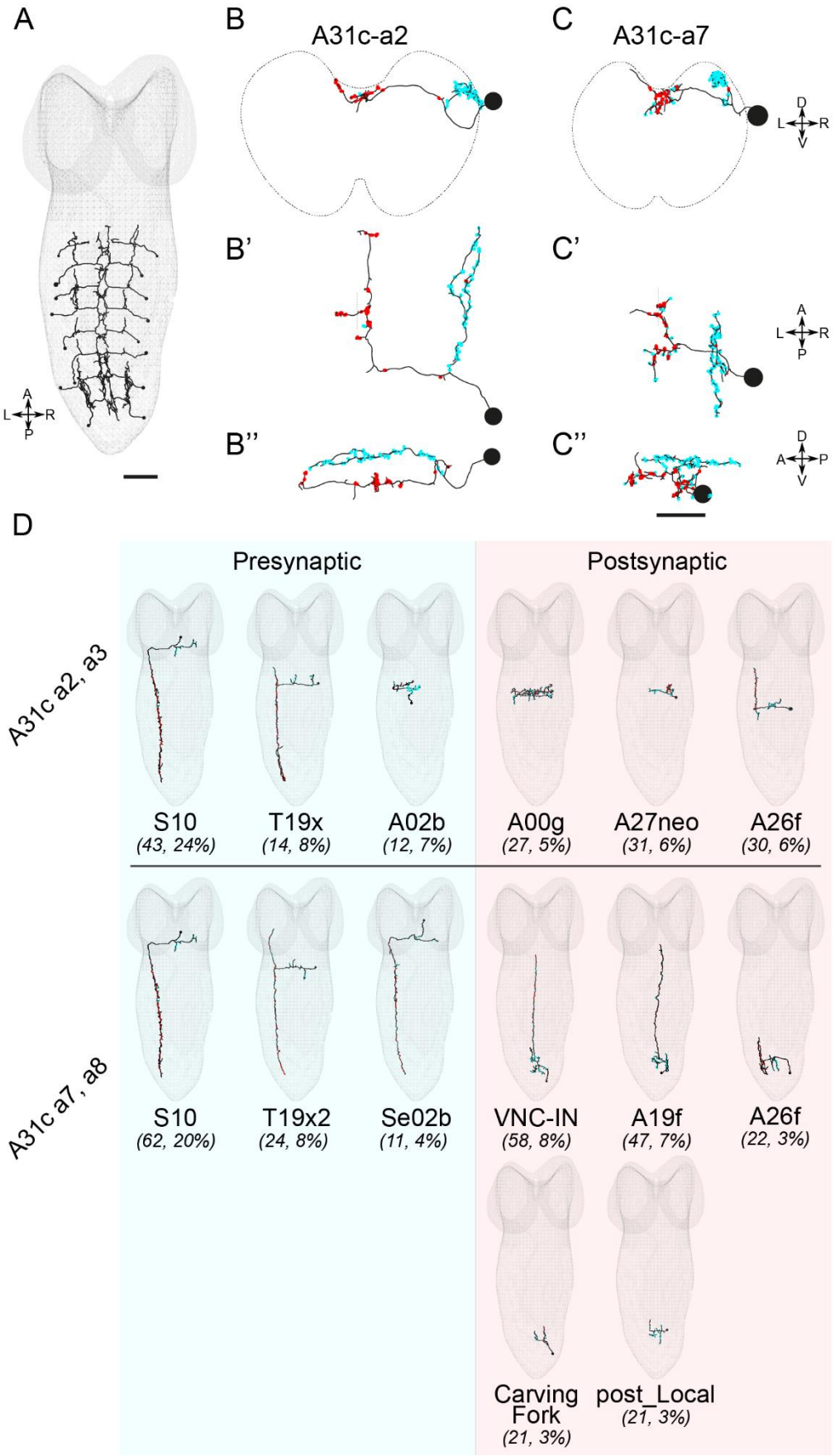

Figure 3. EM reconstruction reveals the connectivity of A31c neurons.

(A) Identification of all A31c neurons in the EM database. Scale bars: 10 µm. **(B)** Morphology of an anterior and a posterior A31c neuron. Red indicates the output sites. Cyan indicates the input sites. **(C)** Example EM images of a presynaptic site of A31c neuron. Scale bar: 0.5 µm. **(D)** Top pre- and post-synaptic partners of anterior and posterior A31c neurons.

Identification of GABAergic premotor neurons A26f showing segmentally synchronized activity preceding the fictive forward wave

Since A26f neurons are postsynaptic to A31c (Figure 3D and Figure 3-supplement C and D) and strongly innervate LT motor neurons (Figure 4A and Figure 4-supplement A; Zarin et al., 2019, Zwart et al., 2016), we next focused on A26f neurons to understand the neural mechanism underlying the generation of the interwave phase. We used a split GAL4 driver ("*A26f-sp*"), which labels A26f neurons in neuromeres A3-A5 (Figure 4B), to investigate their morphology and neurotransmitter identity. A26f neurons have synaptic input sites dorsally near the midline and synaptic output sites near the DL tract (Figure 4B). Remarkably, A26f neurons project their axon along the DL tract for multiple segments. As a representative example, the axon of A26f neuron of neuromere A5 extends four neuromeres from A6 neuromere to A3 neuromere (Figure 4B). We found that A26f neurons are GABAergic (Figure 4-supplement B). It has previously been reported that A26f neurons are corazoninergic (Zarin et al., 2019). However, a comparison of the morphology of A26f neurons with confirmed corazoninergic neurons (Santos et al., 2007) and the absence of peptidergic dense core vesicles in A26f neurons in the EM connectomics dataset suggest that A26f neurons are not corazoninergic. A26f neurons form inhibitory synapses to MNs innervating LT muscles in multiple neuromeres, which suggests the potential of the A26f neurons to control the activity of LT muscles broadly in multiple segments.

Next, we related the activity patterns of A26f neurons to behavior by performing dual-color imaging experiments of *A26f-sp>UAS-CD4::GCaMP6f* and *nSyb-LexA>LexAop-*

306 *RGECO1* in the isolated CNS (Figure 4C and Figure 4-supplement C and D; Materials and
307 methods for further details). Unlike most neurons showing fictive wave-like activity (Lemon
308 et al., 2015), A26f neurons only have synchronized activity in neuromeres A3-A5, which
309 mostly occurred during the periods out of the fictive waves (Figure 4C and 4D). Consistent
310 with synchronized activity, there are high correlations between the activity of A26f segmental
311 homologs, unlike pan-neuronal activity (Figure 4E). The A26f neurons can exhibit one or
312 several peaks at the initiation phase of the FW (Figure 4C and 4D). To sum, A26f neurons
313 have four important characteristics: (1) They form inhibitory synapses with motor neurons in
314 multiple segments targeting transverse muscles; (2) A26f neurons in the abdominal
315 segments are activated simultaneously; (3) A26f neurons are activated between wave
316 phases; (4) they are postsynaptic to A31c neurons.
317 As both A26f and A31c neurons show robust synchronous activity at the initiation of
318 FW, we then monitored the activity of the two neurons simultaneously by using *A31c-*
319 *LexA>LexAop-jRGECO1b, A26f-sp>UAS-CD4::GCaMP6f*. We found that the synchronous
320 peak of A26f neurons is “bookended” by the peaks in A31c activity of neighboring segments
321 (Figure 4F). This is consistent with the inhibitory nature of the A31c-A26f synapses and
322 suggests these cell types might be involved in determining the duration of the interwave
323 phase.
324

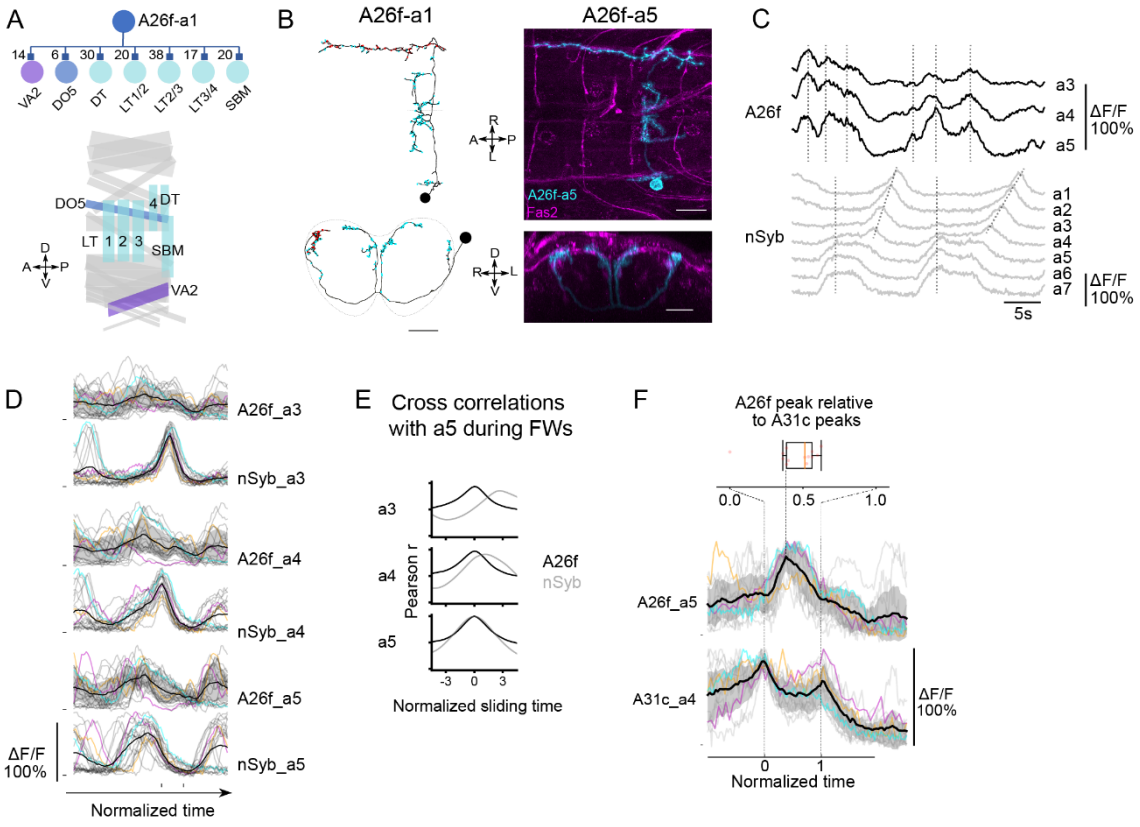

Figure 4. A26f neurons inhibit motor neurons and exhibit synchronous activity at the initiation of forward locomotion

(A) A26f neurons innervate motor neurons. (Top) Postsynaptic neurons of A26f neurons revealed by connectomics analysis in A1 neuromere (Zarin et al., 2019). (Bottom) Layout of body wall muscles in a hemi-segment. Purple, blue, and sky blue muscles are innervated by motor neurons in the same color in the top panel. **(B)** Morphology of A26f neurons shown by the EM reconstruction and confocal images. Scale bars: 20 μm. **(C)** Recording of calcium activity of A26f neurons (*A26f-sp>UAS-CD4::GCaMP6f*) and group activity (*nSyb-LexA>LexAop-RGECO1*). **(D)** Group data of calcium imaging of A26f neurons and nSyb neurons. Each trace is aligned activity peak of nSyb_a4 and nSyb_a2 and normalized to 0-1 by the activity maximum and minimum of the whole recording. Black lines represent the average calcium activity. Shading represents the standard error. Colored lines represent the three example traces. Grey lines represent all other traces. Ticks along the horizontal axis indicate the activity peaks of nSyb_a4 and nSyb_a2. Ticks along the vertical axis indicate the 0. **(E)** Cross correlation of neuronal activity between the neuron in each segment (A3-A5) and the one in A5 (black: A26f neurons, grey: nSyb neurons). See

Materials and methods for details. **(F)** Simultaneous calcium imaging of A31c and A26f neurons. (Bottom) Recording of calcium activity of A26f-a5 neuron (*A26f-sp>UAS-CD4::GCaMP6f*) and its presynaptic partner A31c-a4 neuron (*A31c-LexA>LexAop-jRCaMP1b*) (n = 13 traces, 7 larvae). Colored lines indicate the example traces. Black lines indicate the average calcium activity. Grey lines indicate all other traces. (Top) Peak time of A26f signals relative to the first peak time of A31c signals.

Activation of A26f neurons reduced the amplitude of LT muscle contraction during the forward crawling

To assess whether A26f neurons can inhibit the activity of LT muscles, we analyzed muscle responses to the optogenetic activation of A26f neurons in forward cycles. We combined the optogenetic activator *UAS-CsChrimson* targeted by *A26f-sp* to activate the A26f neurons and the muscle genetic marker *mhc-GFP* expressing GFP to visualize the body wall muscles (*A26f-sp>UAS-CsChrimson, mhc-GFP*). We used *A26f-sp* negative animals as a control (*UAS-CsChrimson*, *mhc-GFP*). Because of the spectral overlap between the light to activate CsChrimson and that to excite GFP, we used a confocal microscopy system that separates the light for optogenetics and imaging into two sections of the objective back aperture, respectively in combination with a new preparation called sideways preparation (Figure 5A and 5B; Materials and methods for detail).

We tracked the length of muscle LT2 and longitudinal muscle VL2 in segment A5 upon optogenetic stimulation. Activation of the A26f neurons reduced the contraction amplitude of the LT2 muscle, while the contraction of the VL2 muscle was almost unchanged (Figure 5C, 5D, and Figure 5-supplement A). These results confirm that activation of A26f neurons is sufficient for the inhibition of the contraction of LT muscles.

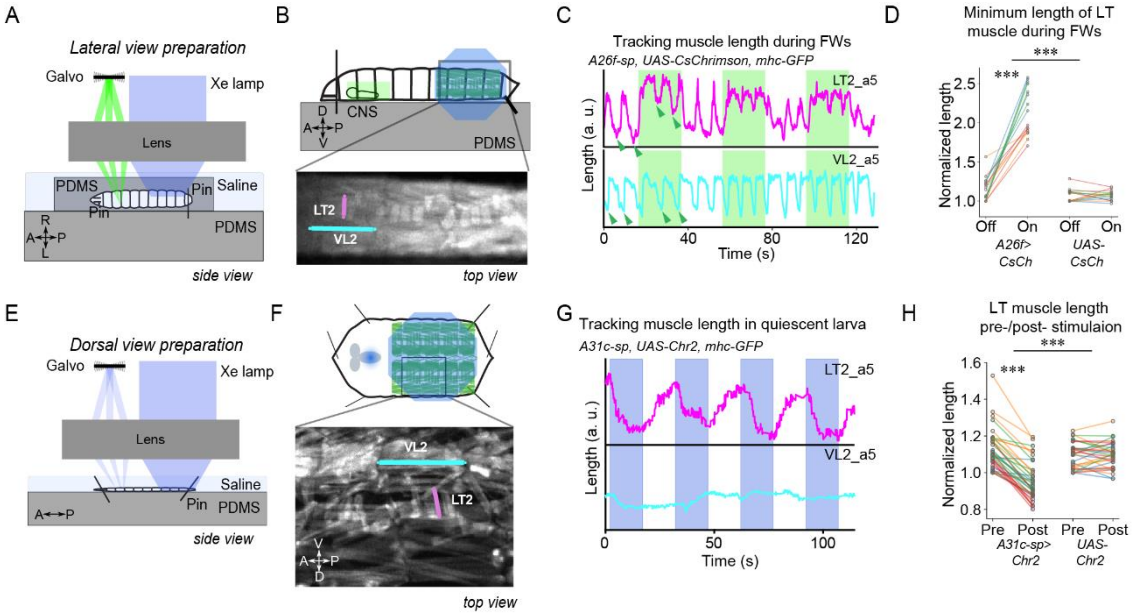

Figure 5. Optogenetic activation of A31c or A26f neurons affects the contraction of LT muscles

(A-D) Optogenetic activation of A26f neurons reduces the contraction amplitude of the LT2 muscle during forward crawlings in the sideways preparation. **(E-H)** Optogenetic activation of A31c neurons causes contraction of the LT muscle in the fillet preparation. **(A and E)** Experimental setups. See Materials and methods for details. **(B and F)** Schematics of the imaging setup (top) and sample fluorescence images (bottom). **(C and G)** Traces of the length of the transverse muscle LT2 and the longitudinal muscle VL2 in the optogenetic experiments. Shaded regions show the timing when the light stimulus is applied. Arrowheads indicate where the measurement was made in Figure 5D. **(D)** The minimum length of the LT2 muscle was increased by the activation of A26f neurons. Muscle lengths are normalized to the minimum length during the light-off period. The hierarchical bootstrap test (See Material and methods for details.) **(H)** The length of the LT2 muscle in the resting state was decreased by the activation of A31c neurons. Muscle lengths are normalized to the minimum length during the light-off period. The hierarchical bootstrap test (See Material and methods for details.)

Activation of A31c neurons induced the contraction of LT muscles

As A31c could inhibit A26f based on the connectivity (Figure 3D and Figure 2-

supplement A) and activity (Figure 4G') analyses described above, we tested whether activation of A31c neurons can enhance contractions of LT muscles. We therefore activated A31c neurons and analyzed the change in LT2 muscle length using animals carrying *A31c-sp>UAS-Chr2.T159C, mhc-GFP* transgenes. We restricted the stimulation laser to the abdominal neuromeres in a semi-intact preparation ("fillet preparation", Pulver et al., 2015) to avoid activating SEG or brain neurons (Figure 5E and 5F). The stimulation caused the contraction of LT muscles in all visualized abdominal neuromeres (A3-A8; Figure 5G), causing a reduction in the minimum length of the LT2 muscle (Figure 5H). These results suggest that activation of A31c neurons is sufficient to activate the LT muscles. As no apparent contraction of other muscles was observed (Figure 5-supplement B), we assume that the A31c neurons mainly regulate the activity of the LT muscles.

Silencing A31c or A26f neurons influenced the amplitude of the LT muscle contraction during forward crawling

Next, we examined if the interneurons of interest were required for the observed contraction of the LT muscles. To test this, we used optogenetic silencing combined with muscular imaging in the sideways preparation (Figure 5A). We first tested whether A26f neurons are required for the contractions of transverse muscles by using animals carrying *A26f-sp>UAS-GtACR1, mhc-GFP* for optogenetic silencing and muscular visualization. We found that the minimum length of muscle LT2 decreased after optogenetic silencing of A26f, suggesting increased levels of contraction (Figure 6A and 6B). We next assessed the requirement of A31c neurons by using *A31c-sp>UAS-GtACR1, mhc-GFP*. We found that after optogenetic silencing, the minimum length of the LT2 muscle in segment A5 was increased during forward cycles (Figure 6A and 6B). The minimum length of transverse muscle VL2 was not affected by the inhibition of A26f or A31c (Figure 6C). These results reveal that the activity of A26f and A31c neurons is both necessary and sufficient for the appropriate contractions of LT muscles observed during locomotor cycles.

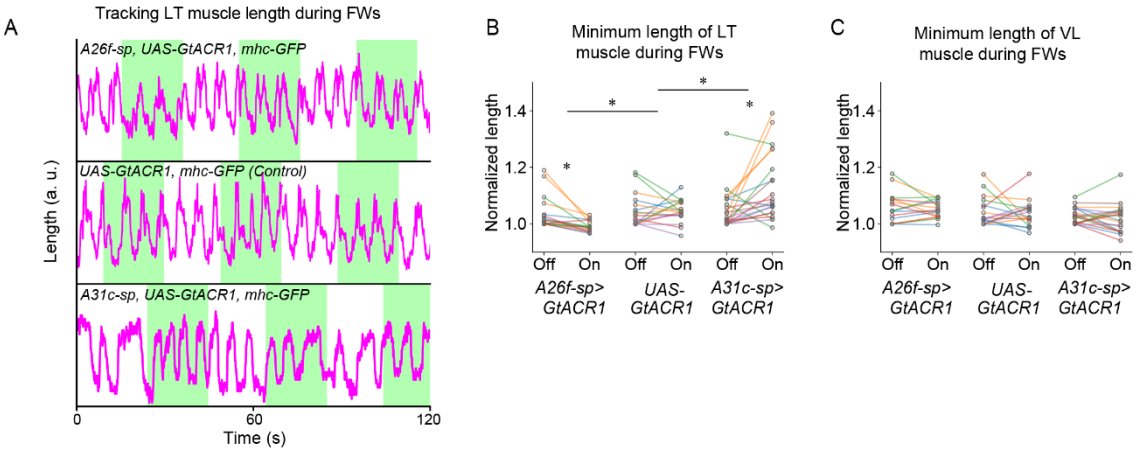

Figure 6. Optogenetic inhibition of A31c or A26f neurons affects the contraction of LT muscles

(A) Traces of the length of transverse muscles (LT2) in the sideways preparation with optogenetic stimulation. **(B)** The minimum length of LT muscles was affected by the optogenetic inhibition of A31c or A26f neurons. Muscle lengths are normalized to the minimum length during the light-off period. The hierarchical bootstrap test (see Material and methods for details.) **(C)** The minimum length of VL muscles was not affected by the optogenetic inhibition of A31c or A26f neurons. Muscle lengths are normalized to the minimum length during the light-off period.

A26f neurons modulate interwave duration

Our previous results suggest that the activation of A26f neurons reduces the contraction of the LT muscles, thereby potentially reducing the duration of the interwave phase. To test this hypothesis, we activated A26f neurons and analyzed the kinematics of crawling in animals of the genotype *A26f-sp>CsChrimson* on low-concentration agarose plates (0.7%) (Figure 7A and 7B). We used animals that lacked the *A26f.DBD* transgene as a control (*A26f.AD>CsChrimson*).

During optogenetic activation of A26f neurons, larvae exhibited faster crawling (Figure 7B). By analyzing the kinematics, we confirmed that the interwave phase and the

total stride duration were both significantly decreased during the optogenetic activation (Figure 7C and 7C'). On the other hand, the wave duration was slightly increased (Figure 7-supplement A). Consistent with these results, the speed of crawling was significantly increased (Figure 7C''). These results suggest that the activation of A26f neurons is sufficient to increase stride frequency and speed.

Next, we asked if A26f neurons are required to regulate the interwave phase and thereby the speed of freely crawling animals. To this end, we optogenetically inhibited A26f neurons in animals carrying *A26f-sp>GtACR1* and analyzed their crawling kinematics (Figure 7D-D'' and Figure 7-supplement C and D). We found that inhibiting the A26f neurons increased the interwave duration and stride duration but had no significant effect on the wave duration (Figure 7D, 7D' and Figure 7-supplement C), resulting in decreased speeds (Figure 7D''). Combined with our previous analyses, these results indicate that the A26f neurons are functionally required to regulate the speed of locomotion by modulating the contraction of LT muscles.

Activation of A31c neurons caused the increase in the interwave duration and the stride duration

Next, we tested the effect of manipulating A31c on crawling (Figure 7-supplement C-L). To activate A31c neurons, we used a genetic system *UAS-VNC-CsChrimson* that confines the expression of CsChrimson to the VNC neurons targeted by the *A31c-sp* transgene, resulting in expression in neuromeres A2-A8. We used animals carrying *UAS-VNC-CsChrimson* as a control. During the activation of A31c neurons, the interwave duration and the stride duration were significantly increased, while no significant difference was found in the wave duration (Figure 7-supplement E, F, and H). These effects are consistent with those observed in the inhibition of A26f neurons (Figure 7D, 7D', and Figure 7-supplement C). On the other hand, the perturbation of A31c neurons could not induce other phenotypes in crawling kinematics (Figure 7-supplement G and I-L), which implies the involvement of

459 other presynaptic neurons to A26f neurons in speed control. Consequently, these data imply
460 that A31c neurons should contribute to the regulation of interwave phase duration through
461 A26f neurons by the multi-segmental synchronous excitation within the interwave phase.

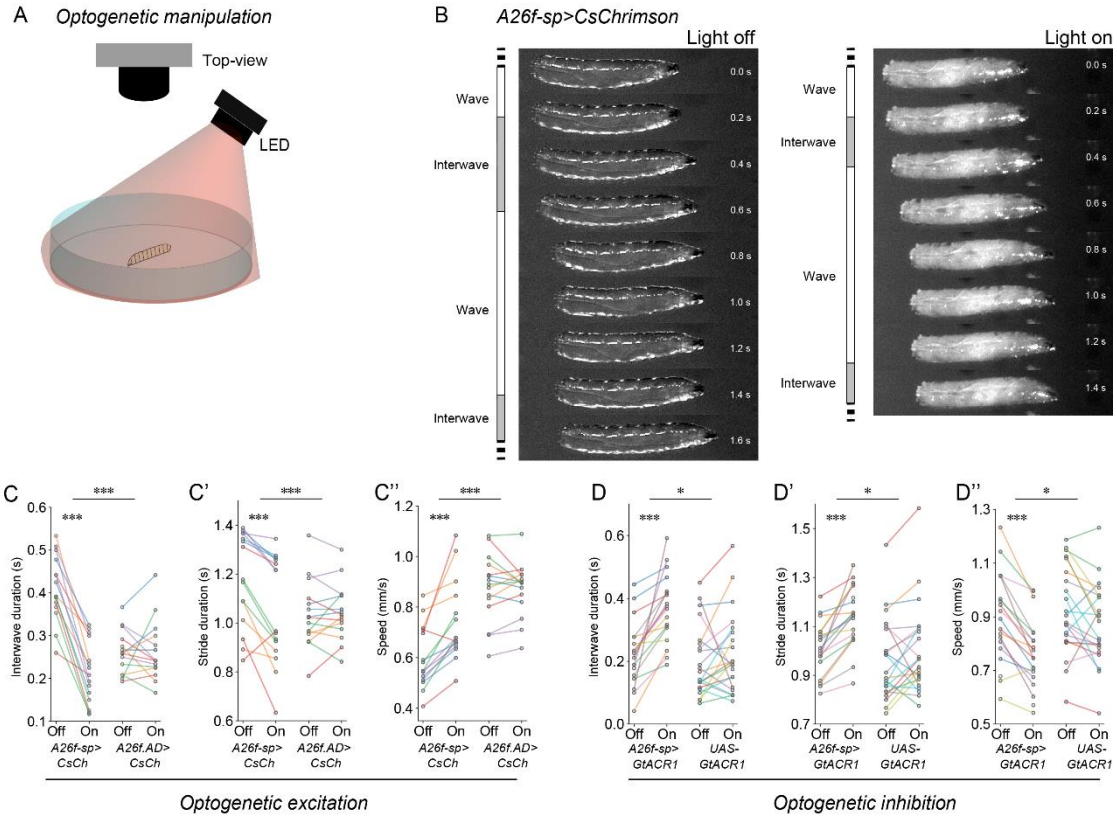

462

463 **Figure 7. Optogenetic manipulation of A26f neurons affects the interwave duration**

464 **(A)** Experimental setup for optogenetics in free-crawling larvae. **(B)** Example frames show that
465 the interwave phase is reduced during the activation of A26f neurons. **(C-C'')** Crawling dynamics
466 changed during the activation of A26f neurons. The hierarchical bootstrap test (See Material and
467 methods for details.) **(D-D'')** Crawling dynamics changed during the inhibition of A26f neurons.
468 The hierarchical bootstrap test (See Material and methods for details.)

469

470

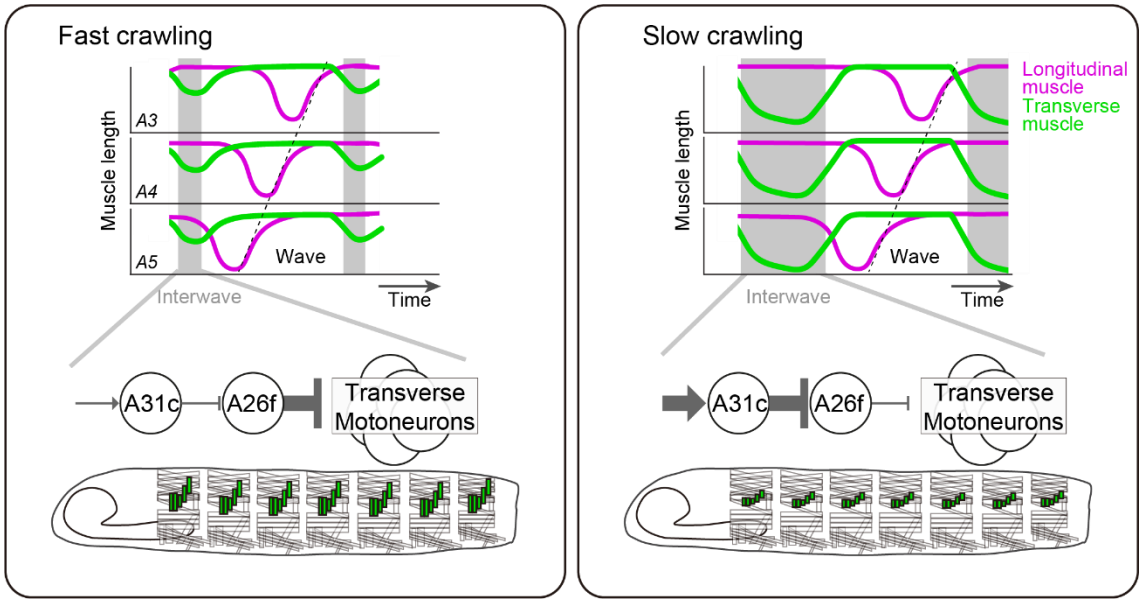

Figure 8. Schematics of larval speed control.

Contraction of transverse muscles is suppressed by A26f neurons to make the interwave phase short and crawl fast (left panel). Multi-segmental synchronous activity of A31c and A26f neurons elongates the interwave phase duration to decrease crawling speed (right panel).

Discussion

In summary, we aimed to understand the neural mechanisms that underlie the selective modulation of one phase of the locomotor cycle. We used the *Drosophila* larva as a model and found that this animal uses a strategy to primarily vary the phase between consecutive peristaltic waves for speed regulation. To implement this strategy, the larva modulates the amplitude and duration of the contraction of the LT muscles that are perpendicular to the crawling direction, which contract synchronously along the anterior-posterior axis before the onset of the peristaltic wave. The GABAergic interneurons A26f and A31c, upstream of the MNs innervating the LT muscles, showed segmentally synchronized activity preceding the FW. Connectivity analysis further revealed that A31c neurons receive shared descending input, and synapse onto ascending neurons and local neurons, including A26f. A26f neurons are sufficient and required for the desired activity of the LT muscles and thus the interwave duration and speed. Altogether, we established a neural basis for speed

490 regulation by linking the speed-dependent modulation of contractions of muscles to the
491 interneurons that control their activity (Figure 8).
492
493 **Mechanics/mechanisms of modulating speed of locomotion**
494 Locomotion speed is a function of the frequency and length of a cycle. We found that,
495 similar to previous findings, the speed of larval crawling is determined more so by stride
496 frequency than stride length (Frigon et al., 2014; Grillner et al., 1979; Jacobson and Hollyday,
497 1982; Nirody et al., 2021). Furthermore, similar to limbed animals including mammals and
498 other insects, the two constituent phases of a locomotor cycle vary differentially with speed,
499 with the interwave phase varying more than the wave phase. This similarity between the
500 dynamics of locomotion between limbed and axial locomotion could be indicative of the
501 kinematic constraints of each type of movement. For limbed locomotion, the forces required
502 to move the limb during the swing phase depend on the limb's mass. Large limbed animals,
503 such as horses and humans (Boije and Kullander, 2018; Minassian et al., 2017), could use
504 momentum-based strategies, requiring only brief active contractions in swing muscles,
505 whereas smaller animals such as stick insects and mice (Bellardita and Kiehn, 2015; Bidaye
506 et al., 2018) require constant neural input onto the swing muscles. In both cases, the relative
507 invariance of the duration of this phase suggests that the rotational inertia of swinging limbs
508 may be an important limiting factor in limbed locomotion (Kilbourne, 2013; Kilbourne and
509 Hoffman, 2013, 2015; Rocha-Barbosa et al., 2005). The relative invariance of the wave
510 phase suggests a similar constraint on the *Drosophila* larval motor system. Furthermore, the
511 transverse muscle contractions during the interwave phase may be an evolutionary
512 adaptation, with an additional set of neurons that control it. Consistent with this hypothesis,
513 the last common ancestor to all bilaterians, the so-called "Urbilaterian", is thought to have
514 only had circular and longitudinal muscles (Cannon et al., 2016), and transverse muscles
515 have only been identified in the larvae of some other species of Diptera (e.g., *T. castaneum*,
516 Schultheis et al., 2019; *G. mellonella*, Emery et al., 2019). Furthermore, the transverse

517 muscles are under independent neuromodulatory control (Elliott et al., 2021), and their motor
518 neurons are innervated by a distinct set of interneurons (Zwart et al., 2016, Kohsaka et al.,
519 2019).

520 In addition to the kinematic and evolutionary constraints, the differential modulation
521 of the locomotor cycle may have several advantages. First, it could be a more efficient control
522 strategy: independent control of the extension of the head and the peristaltic wave may
523 reduce the complexity of motor control, and increase the flexibility of the head and tail by
524 allowing the two ends to be moved separately. This may be particularly important as the
525 anterior-most segments are involved in other motor programs including feeding (Melcher and
526 Pankratz, 2005), and the transverse muscles control self-righting behaviour (Picao-Osorio et
527 al., 2015). Second, it could improve energy efficiency within a particular range of speeds:
528 though the contraction and extension of LT muscles during the movement of the head must
529 entail a metabolic cost, the energy cost of moving the center of mass (CoM) might be reduced
530 during slower movements. The CoM is mainly moved in the pistoning phase during the head
531 extension and the tail contraction (Heckscher et al., 2012), and the transverse muscle
532 contractions, which we speculate are involved in driving head movements, might be a more
533 efficient method of extending the anterior segments by regulating the hydrostatic skeleton
534 (Trimmer and Issberner, 2007).

535

536 **Neuronal control of speed modulation**

537 A large body of work has identified the neural basis of the regulation of speed of
538 locomotion in vertebrates, identifying associated circuits across the brain and spinal cord.
539 Mouse, zebrafish, and Xenopus spinal cord preparations have been used to describe the
540 selective recruitment of specific interneuron and motor neurons at different speeds (Berg et
541 al., 2018; Boije and Kullander, 2018; Gatto and Goulding, 2018; Grillner and El Manira, 2020;
542 Grillner and Kozlov, 2021; Kiehn, 2016; Roberts et al., 2010). These neurons are
543 interconnected between members of the same “module”, each of which is sequentially

recruited as the animal adjusts its speed of locomotion. Neuromodulation tunes the recruitment of neurons within these modules in the adjustment of speed during locomotion (Jha and Thirumalai, 2020). In limbed animals, changes in speeds are often accompanied by changes in gait (Bellardita and Kiehn, 2015). How the corresponding qualitative and quantitative changes in the locomotor cycle are achieved, is an area of active research. In the mouse spinal cord, V2a interneurons are required for maintaining left–right alternation at high-speed trotting (Crone et al., 2009). Furthermore, commissural $V0_V$ neurons are necessary for trot at all speeds, and ablation of commissural $V0_V$ and $V0_D$ neurons abolishes walk, trot, and gallop gaits (Bellardita and Kiehn, 2015). In the brainstem, the mesencephalic locomotor region (MLR) controls the initiation of locomotion and the expression of specific gaits. The MLR's cuneiform nucleus (CnF) and the pedunculopontine nucleus (PPN) mediate alternating locomotor stepping in mice, whereas the CnF alone is necessary for high-speed synchronous locomotion such as found in galloping (Caggiano et al., 2018). A recent study identified distinct subclasses of glutamatergic neurons within the MLR, each with distinct roles in motor control outside of locomotion (Ferreira-Pinto et al., 2021), suggesting this nucleus has wider roles in regulating behavior. Despite this recent attention to the modulation of the speed of locomotion, the neural basis of the differential modulation of the locomotor cycle is still unknown. We have uncovered a set of inhibitory neurons, whose activity determines the duration of the interwave phase, thereby setting the frequency of locomotion. The inhibitory nature of this set of cells to regulate muscle contractions has many parallels in other systems. One of the simplest circuit designs for rhythm generation, the 'half-center oscillator', relies on reciprocal inhibition to generate alternating patterns of activity (Marder and Bucher, 2001), and reciprocal inhibition within the spinal cord is thought to underlie the generation of alternation during locomotion (Deliagina and Orlovsky, 1980; Geertsen et al., 2011; Pratt and Jordan, 1987). Indeed, inhibitory neurons shape the rhythms of neural activity on different timescales in systems from crustacean stomatogastric ganglion to vertebrate cortical circuits (Cardin, 2019; Marder and Bucher, 2001). In addition, a parallel between the

Drosophila larval system and limbed locomotion can be seen in the mechanics of movement. For instance, in cats, the extensor muscles are mainly activated during the stance phase, while the flexor muscles are mainly activated in the swing phase (Engberg and Lundberg, 1969); similarly, we found that the fruit fly larva contracts its transverse muscles during the interwave phase, and its longitudinal muscles during the wave phase. These parallels may be mirrored within the neural circuitry mediating these muscle contractions. While the detailed implementation will obviously differ, the inhibitory neural circuit motif underlying the generation of the asymmetry of the two constituent phases of locomotion could therefore be conserved between species.

Materials and methods

Fly strains

Except where specifically mentioned, larvae were raised in standard cornmeal-based food at room temperature (25 °C), and third instar larvae were used for experiments. We used the following *all-trans* retinal (ATR) feeding conditions for optogenetics: 10 mM ATR yeast from 18 to 36 hours in CsChrimson and Channelrhodopsin 2 (Chr2.T159C) groups, 3 mM ATR yeast from 24 to 48 hours in GtACR1 groups. Fly strains are listed in Table 1. We used the split GAL4 drivers *A31c-a8-sp* (*R24H08-GAL4.AD*, *R45F08-GAL4.DBD*), *A31c-sp* (*R41F02-GAL4.AD*, *R44F09-GAL4.DBD*), and *A26f-sp* (*VT050223-GAL4.AD*, *R15E05-GAL4.DBD*). Transgenic flies *nSyb-LexA* were generated in the lab. The enhancer sequence of *neuronal Synaptobrevin (nSyb)* (*R57C10*, Pfeiffer et al., 2012) was cloned into pBPLexA::p65Uw plasmid (Pfeiffer et al., 2010). The transgenic line was generated in the *VK00027* locus (BestGene Inc., USA). Sources of the fly strains are listed in Table 1.

Immunostaining and calcium imaging

We used a standard immunostaining procedure (Kohsaka et al., 2014). First, the

598 larvae were dissected in the fillet preparation, fixed in 4% formaldehyde for 30 min at room
599 temperature, washed twice with 0.2% Triton X-100 in PBS (PBT) for 15 min at room
600 temperature, blocked with 5% normal goat serum in PBT for 30 min at room temperature,
601 and stained with the first antibody at 4 °C for 24 to 48 hours. After that, the preparations were
602 washed twice with PBT for 15 min and stained with the second antibody at 4 °C for 24 to 48
603 hours. Sources and concentrations of antibodies are listed in Table 1.

604 In the calcium imaging of the isolated CNS, the CNS of third instar larvae was
605 dissected out (Kohsaka et al., 2014), transferred to a drop of TES buffer (TES 5 mM, NaCl
606 135 mM, KCl 5 mM, $MgCl_2$ 4 mM, $CaCl_2$ 2 mM, sucrose 36 mM; pH = 7.15), and attached
607 dorsal-up on MAS-coated slide glass for imaging (Matsunami Glass, Japan). GCaMP6f
608 fluorescence was detected by a spinning-disk confocal unit (CSU21, Yokogawa, Japan) and
609 an EMCCD camera (iXon, Andor Technology, Germany) on an upright microscope,
610 Axioskop2 FS (Zeiss, Germany). We used a dual-view system (CSU-DV, Solution Systems,
611 Japan) to perform dual-color calcium imaging for GCaMP and R-GECO1.
612
613 **Top-view crawling assay and analysis**

614 Third instar wandering larvae of *sr-GAL4>GFP* (about 0-4 hours after the start of
615 wandering) were used. We transferred a larva onto an agarose plate of a standard
616 concentration (1.5%), waited for about 1 minute, and took a video for 5 minutes. An Olympus
617 stereomicroscope (SZX16, Olympus, Japan) and a 0.7x lens were used for magnification. A
618 CMOS camera (C11440-22CU, Hamamatsu Photonics, Japan) was used for video recording.
619 A square of 1.6 x 1.6 cm of 1024 x 1024 pixels was recorded. The frame rate was set at 30
620 Hz. A mercury lamp (U-HGLGPS, Olympus, Japan) and an excitation filter (460-495 nm)
621 were used to deliver ~ 5 μW/mm^2 of blue light for illumination.

622 We reviewed all videos to extract episodes of straight runs of more than three strides.
623 We then randomly selected three episodes for each larva and analyzed the stride parameters.
624 An ImageJ script was used to manually annotate the video to obtain kinematic parameters

(version 1.53, Abràmoff et al., 2004). The stride length was obtained from the distance between the landing positions of the prominent ventral denticle at A8 on one lateral side. The stride duration was obtained from the duration between the unhooking moments. The time of wave initiation was annotated when the A8 prominent denticle moved half a segmental length.

To model the relationship between the stride duration and the duration of the two constituent phases, we tested the polynomial models and the piecewise linear model with two pieces. We then compared the Bayesian information criterion (BIC) between these models (Burnham and Anderson, 2004). The BIC is defined as

$$BIC = K\,ln(n) - 2\,ln(\hat{L}).$$

K is the number of estimated parameters in the model. n is the amount of data. $\hat{L}$ is the maximum value of the likelihood function for the model. In the case of least squares estimation with normally distributed errors, BIC can be expressed as

$$BIC = K\,ln(n) + n\,ln(\hat{\sigma}^2),$$

where $\hat{\sigma}^2$ is the average of the squares of residuals. We calculated the BIC for the linear piecewise model of two pieces and the polynomial models of degrees from 2 to 10. The BIC has a minimum value with the cubic polynomial model.

Side-view imaging of the muscular ends and analysis

Third instar wandering larvae (about 0 to 12 hours after starting wandering) were used. An agarose plate of a standard concentration (1.5%) with black ink (0.2%) was used as the substrate. We oriented a CMOS camera (C11440-22CU, Hamamatsu, Japan) and its zoom lens (MLM3X-MP, Computar, Japan) with a 2x extender (FP-EX2, RICOH, Japan) horizontally for recording. Each time one larva was transferred to the agarose plate for recording. We manually moved the plate to let the camera focus on the larval body wall. The top-view imaging was simultaneously recorded with the same instrument described in the previous method section. A mercury lamp (U-HGLGPS, Olympus, Japan) and an excitation

652 filter (460-495 nm) were used to deliver 5 μW/mm^2 of blue light for the illumination of the
653 GFP-tagged tendon cells. We recorded at 30 Hz for about 3 minutes and typically collected
654 3-5 episodes in focus. Each episode includes 2-5 straight crawls.

655 To analyze the kinematics of the muscular movement, we used DeepLabCut (Mathis
656 et al., 2018) to track the muscular ends. We labeled the muscular ends for 40-50 frames in
657 each video and trained the resnet50 network with the labeled frames for 1,000,000 iterations.
658 To understand the relationship between the contraction of LT muscles and the head and tail
659 movement, an ImageJ script was used to obtain the minimum/maximum length of the LT2
660 muscle, the maximum thoracic length, the tail traveling distance, and the interwave duration
661 (version 1.53, Abràmoff et al., 2004). To obtain the minimum/maximum length of the LT2
662 muscle, we annotated the position of the muscular ends of the LT2 muscle in segments A2-
663 A7 when they were mostly contracted and extended and calculated the distance of the pairs
664 of muscular ends. To obtain the maximum thoracic length, we annotated the anterior end of
665 the head and the central point of the T3/A1 segmental boundary at the dorsal side and
666 calculated the distance between them. To obtain the tail traveling distance, we annotated the
667 landing positions of the tail and calculated the distance. The interwave duration was obtained
668 as described in the previous section.
669
670 **Trans-synaptic tracing by *trans*-Tango**
671 As *trans*-Tango expression is leaky in larval ventral nerve cord (VNC) neurons when
672 using the recommended rearing temperature 18 °C (Talay et al., 2017), *trans*-Tango larvae
673 were incubated at 30 °C for one day before the experiment. *trans*-Tango expression was
674 thereby restricted to a small number of neurons in combination with the split GAL4 driver
675 *A31c-a8*. We then identified each single neuron by comparing its morphology to the EM
676 database (Ohyama et al., 2015).
677

678 **EM reconstruction**

679 Serial sectioning transmission electron microscopy (ssTEM) data were analyzed as
680 described in Ohyama et al., 2015. Briefly, reconstructions were made in a modified version
681 of CATMAID (Saalfeld et al., 2009; http://www.catmaid.org). LT motoneurons and their
682 presynaptic partners had been identified and reconstructed previously within the ssTEM
683 volume (Zwart et al., 2016). These reconstructions were used to identify and reconstruct all
684 presynaptic partners.

685

686 **Measurement and quantification of calcium activity**

687 To analyze calcium imaging data, we manually circled regions of interest (ROIs)
688 using ImageJ (version 1.53, Abràmoff et al., 2004). ROIs were chosen at the medial dendritic
689 sites for the A26f neurons, at the axons for the A31c neurons, and the neuropil for the pan-
690 neuronal line in each neuromere. To compare the calcium imaging of different forward cycles,
691 we normalized the time in Figure 2D and Figure 4D relative to the peak ΔF/F of nSyb in
692 segments A4 and A1. We normalized the time in Figure 4F' relative to the peak ΔF/F of A31c
693 in A4 preceding the FW and the peak ΔF/F of A31c in A4 during the FW. To obtain the time-
694 lagged cross correlation, we slide a trace of calcium activity as in Figure 2D or Figure 4D,
695 calculated the Pearson correlation coefficients with traces of calcium activity in other
696 segments, and calculated the mean value of correlation coefficients by using Fisher-z
697 correction.

698

699 **Optogenetic assay of free crawling**

700 We assayed the response of larvae to optogenetic stimulation by using the same
701 imaging system as the top-view imaging assay. The background illumination and the light for
702 the optogenetic stimulation were set as the following. In the GtACR1 groups, we used a 590
703 nm LED of ~ 150 μW/mm2 to provide the optogenetic stimulation, while a 660 nm LED
704 (M660L3, Thorlabs, USA) or an infrared light (LDQ-150IR2-850, CCS, Japan) provided the

705 background illumination. In the CsChrimson groups, we used an 850 nm infrared light (LDQ-
706 150IR2-850, CCS, Japan) of ~ 40 μW/mm2 to provide the background light and used the 660
707 nm LED to apply the optogenetic stimulation of ~ 60 μW/mm2. We used an ImageJ script to
708 manually annotate videos to obtain the kinematic parameters (version 1.53, Abràmoff et al.,
709 2004). In the experiments using GtACR1, the larva can show transient turning or stopping
710 responses to 590 nm light. In these groups, we analyzed strides if forward cycles were not
711 halted or after forward cycles were reinitiated. In the experiment using *A26f-sp* drivers, we
712 only analyzed the data when the *GtACR1/CsChrimson* was expressed in more than four A26f
713 neurons, which was determined by post-hoc staining.
714
715 **Assay of muscular response to optogenetic stimulation in the fillet and sideways**
716 **preparation**
717 We used a semi-intact fillet preparation to assay muscular responses to optogenetic
718 activation (Kohsaka et al., 2014). After the preparation, we waited for about 10 minutes, until
719 the larva stopped its frequent spontaneous axial waves.
720 To constrain the movement of the larva without impairing peristaltic behavior and
721 visualize the lateral side of the larva, we devised a new preparation named sideways
722 preparation. In this preparation, the larva is fixed by two pins on a vertical side of a
723 Polydimethylsiloxane (PDMS; Silpot 184, Toray, Japan) plate and oriented lateral side up to
724 visualize the LT muscles. The larva can show spontaneous forward peristalsis-like behavior
725 in this preparation. In the preparation, we prepared a PDMS plate with a standing PDMS
726 island filled with 4°C TES buffer, transferred a larva to the PDMS plate, and used two pins to
727 fix the head and tail of the third instar larvae (Figure 5A and 5B). The tail was pinned to the
728 bottom PDMS substrate to make the pin perpendicular to the larval sagittal plane with two
729 pricking points close to the two prominent lateral denticles in the A8 segment. The head was
730 pinned to the PDMS island to make the pin perpendicular to the larval frontal plane. After
731 pinning, the PDMS island was attached to the tail pin and supported the ventral larval body.

4°C TES buffer was used to reduce the larval motion during the preparation. We changed the buffer to 25 °C before imaging.

A local stimulation microscope was used for muscular imaging and optogenetic stimulation (Matsunaga et al., 2013; Takagi et al., 2017). The microscope (FV1000, Olympus, Japan) has two separate optical paths for muscular imaging and optical stimulation, respectively: blue light from a Xeon lamp (X-Cite exacte, Excelitas Technologies, US) and a GFP dichroic mirror (U-MGFP/XL, Olympus, Japan), which were used to image the muscles in the abdominal segments A3/A4 to A7/A8, and a scanning laser of blue (488 nm) or green (559 nm) light, which was used to stimulate the CNS optogenetically. A dichroic mirror separates the two optical paths. To fit the larva into the field of view, we used a 4x Olympus objective and a 1 x or a 0.63 x adapter. Muscular contractions were recorded by an EMCCD camera (iXon, Andor Technology, Germany). We used different combinations of optogenetic stimulation and muscular illumination. In the sideways preparation, a rectangular scanning of about 0.85 mm x 0.4 mm by the 559nm laser was used for optogenetic stimulation (~ 20 μW/mm2 for the CsChrimson groups and ~ 40 μW/mm2 for the GtACR1 groups), while blue light of ~ 10 μW/mm2 was used for muscular illumination. In the fillet preparation, a spiral scanning of a radius of ~ 0.3mm by a 488 nm laser was used to activate the Chr2 (~ 400 mW/mm2), while a blue light of ~ 50 μW/mm2 was used for muscular illumination. DeepLabCut (Mathis et al., 2018) was used to track the muscular ends. We labeled the muscular ends in 40-50 frames in each video and trained them using the resnet50 network. The neural network was trained 1,000,000 times.

Statistical tests for the optogenetic experiments

Changes in muscle length were normalized to the minimal muscle length within each animal. Changes in other values (stride duration, stride length, etc.) were directly used for statistical tests. We tested the significance of the changes before and after the optogenetic manipulation and compared the changes between the experimental and the control. As each

animal was treated with optogenetic stimulation multiple times, to increase the statistical power and to avoid Type-I error (false positive), we used hierarchical bootstrapping methods for the comparison before and after the optogenetic stimulation and the comparison between the experimental and control group (Saravanan et al., 2020). To generate the bootstrapped dataset, we resampled data from the experimental dataset 10,000 times. Each time we 1) resample n animals with replacement (n is the animal number in the experiment), and 2) resample $m_1,..,m_n$ trials within animals with replacement (m_i is the number of trials of the resampled animal i in the experiment) (Saravanan et al., 2020). For the comparison before and after the optogenetic stimulation, we used the empirical method by 1) computing the animal-wide mean of the bootstrapped sample μ^*, 2) computing the difference between μ^* and the animal-wide mean of the experiment μ, and 3) computing the p-value as the quantile of μ in $\mu^* - \mu$ (Efron and Tibshirani, 1994). For the comparison between the experimental and control group, we 1) computed the animal-wide mean of the two bootstrapped samples ($\mu^{a,*}$ and $\mu^{b,*}$), 2) computed a joint probability distribution of $\mu^{a,*}$ and $\mu^{b,*}$, and 3) computed the p-value as the density of the joint probability (Saravanan et al., 2020). All analysis was done with Python (version 3.9.12) scripts using the libraries NumPy (version 1.21.5) and SciPy (version 1.7.3). Asterisks represent the range of p values (*p<0.05; **p<0.005; ***p<0.0005).

Acknowledgment

We thank Bloomington *Drosophila* Stock Center, KYOTO *Drosophila* Stock Center, and Drs. Chris Doe, Miki Fujioka, Karen Hibbard, and Cynthia L. Hughes for the fly lines (Table 1). We thank Developmental Studies Hybridoma Bank and Dr. Hermann Aberle for the antibodies. We thank Drs. Stefan Pulver and Wenchang Li for critical comments on the paper. This work was supported by MEXT/JSPS KAKENHI grants (17K19439, 19H04742, 20H05048 to A.N. and 17K07042, 20K06908 to H.K.) and the Royal Society of Edinburgh (grant 64553 to M.F.Z.).

Competing interests

We have no conflicts of interest with respect to the work.

Availability of data and materials

The data generated in this study will be available from the Zenodo repository.

References

Abràmoff MD, Magalhães PJ, Ram SJ. 2004. Image processing with ImageJ. Biophotonics international 11:36–42.

Ampatzis K, Song J, Ausborn J, El Manira A. 2014. Separate microcircuit modules of distinct v2a interneurons and motoneurons control the speed of locomotion. Neuron 83:934–943.

Ampatzis K, Song J, Ausborn J, El Manira A. 2013. Pattern of innervation and recruitment of different classes of motoneurons in adult zebrafish. J Neurosci 33:10875–10886.

Atsuta Y, Garcia-Rill E, Skinner RD. 1990. Characteristics of electrically induced locomotion in rat in vitro brain stem-spinal cord preparation. J Neurophysiol 64:727–735.

Bellardita C, Kiehn O. 2015. Phenotypic characterization of speed-associated gait changes in mice reveals modular organization of locomotor networks. Curr Biol 25:1426–1436.

Berg EM, Björnfors ER, Pallucchi I, Picton LD, El Manira A. 2018. Principles Governing Locomotion in Vertebrates: Lessons From Zebrafish. Front Neural Circuits 12. doi:10.3389/fncir.2018.00073

Berrigan D, Pepin DJ. 1995. How maggots move: Allometry and kinematics of crawling in larval Diptera. J Insect Physiol 41:329–337.

Bidaye SS, Bockemühl T, Büschges A. 2018. Six-legged walking in insects: how CPGs, peripheral feedback, and descending signals generate coordinated and adaptive motor rhythms. J Neurophysiol 119:459–475.

Boije H, Kullander K. 2018. Origin and circuitry of spinal locomotor interneurons generating

different speeds. Curr Opin Neurobiol 53:16–21.

Burnham KP, Anderson DR. 2004. Multimodel Inference: Understanding AIC and BIC in Model Selection. Sociol Methods Res 33:261–304.

Caggiano V, Leiras R, Goñi-Erro H, Masini D, Bellardita C, Bouvier J, Caldeira V, Fisone G, Kiehn O. 2018. Midbrain circuits that set locomotor speed and gait selection. Nature 553:455–460.

Caldwell JC, Miller MM, Wing S, Soll DR, Eberl DF. 2003. Dynamic analysis of larval locomotion in Drosophila chordotonal organ mutants. Proc Natl Acad Sci U S A 100:16053–16058.

Cannon JT, Vellutini BC, Smith J 3rd, Ronquist F, Jondelius U, Hejnol A. 2016. Xenacoelomorpha is the sister group to Nephrozoa. Nature 530:89–93.

Capelli P, Pivetta C, Soledad Esposito M, Arber S. 2017. Locomotor speed control circuits in the caudal brainstem. Nature 551:373–377.

Cardin JA. 2019. Functional flexibility in cortical circuits. Curr Opin Neurobiol 58:175–180.

Crone SA, Zhong G, Harris-Warrick R, Sharma K. 2009. In mice lacking V2a interneurons, gait depends on speed of locomotion. J Neurosci 29:7098–7109.

Dasen JS. 2017. Master or servant? emerging roles for motor neuron subtypes in the construction and evolution of locomotor circuits. Curr Opin Neurobiol 42:25–32.

Deliagina TG, Orlovsky GN. 1980. Activity of Ia inhibitory interneurons during fictitious scratch reflex in the cat. Brain Res 193:439–447.

Efron B, Tibshirani RJ. 1994. An Introduction to the Bootstrap. CRC Press.

Elliott AD, Berndt A, Houpert M, Roy S, Scott RL, Chow CC, Shroff H, White BH. 2021. Pupal behavior emerges from unstructured muscle activity in response to neuromodulation in Drosophila. Elife 10. doi:10.7554/eLife.68656

Emery H, Johnston R, Rowley AF, Coates CJ. 2019. Indomethacin-induced gut damage in a surrogate insect model, Galleria mellonella. Arch Toxicol 93:2347–2360.

Engberg I, Lundberg A. 1969. An electromyographic analysis of muscular activity in the

hindlimb of the cat during unrestrained locomotion. Acta Physiol Scand 75:614–630.

Ferreira-Pinto MJ, Kanodia H, Falasconi A, Sigrist M, Esposito MS, Arber S. 2021. Functional diversity for body actions in the mesencephalic locomotor region. Cell 184:4564-4578.e18.

Friesen WO, Kristan WB. 2007. Leech locomotion: swimming, crawling, and decisions. Curr Opin Neurobiol 17:704–711.

Frigon A, D'Angelo G, Thibaudier Y, Hurteau M-F, Telonio A, Kuczynski V, Dambreville C. 2014. Speed-dependent modulation of phase variations on a step-by-step basis and its impact on the consistency of interlimb coordination during quadrupedal locomotion in intact adult cats. J Neurophysiol 111:1885–1902.

Gatto G, Goulding M. 2018. Locomotion Control: Brainstem Circuits Satisfy the Need for Speed. Curr Biol.

Geertsen SS, Stecina K, Meehan CF, Nielsen JB, Hultborn H. 2011. Reciprocal Ia inhibition contributes to motoneuronal hyperpolarisation during the inactive phase of locomotion and scratching in the cat. J Physiol 589:119–134.

Grillner S. 1985. Neurobiological bases of rhythmic motor acts in vertebrates. Science 228:143–149.

Grillner S. 1974. On the generation of locomotion in the spinal dogfish. Exp Brain Res 20:459–470.

Grillner S, El Manira A. 2020. Current Principles of Motor Control, with Special Reference to Vertebrate Locomotion. Physiol Rev 100:271–320.

Grillner S, Halbertsma J, Nilsson J, Thorstensson A. 1979. The adaptation to speed in human locomotion. Brain Res 165:177–182.

Grillner S, Kozlov A. 2021. The CPGs for Limbed Locomotion–Facts and Fiction. Int J Mol Sci 22:5882.

Hägglund M, Borgius L, Dougherty KJ, Kiehn O. 2010. Activation of groups of excitatory neurons in the mammalian spinal cord or hindbrain evokes locomotion. Nat Neurosci 13:246–252.

867 Hägglund M, Dougherty KJ, Borgius L, Itohara S, Iwasato T, Kiehn O. 2013. Optogenetic
868 dissection reveals multiple rhythmogenic modules underlying locomotion. Proc Natl Acad Sci
869 U S A 110:11589–11594.
870 Heckscher ES, Lockery SR, Doe CQ. 2012. Characterization of Drosophila larval crawling at
871 the level of organism, segment, and somatic body wall musculature. J Neurosci 32:12460–
872 12471.
873 Hiramoto A, Jonaitis J, Niki S, Kohsaka H, Fetter RD, Cardona A, Pulver SR, Nose A. 2021.
874 Regulation of coordinated muscular relaxation in Drosophila larvae by a pattern-regulating
875 intersegmental circuit. Nat Commun 12:2943.
876 Hughes CL, Thomas JB. 2007. A sensory feedback circuit coordinates muscle activity in
877 Drosophila. Mol Cell Neurosci 35:383–396.
878 Jacobson RD, Hollyday M. 1982. A behavioral and electromyographic study of walking in the
879 chick. J Neurophysiol 48:238–256.
880 Jha U, Thirumalai V. 2020. Neuromodulatory Selection of Motor Neuron Recruitment
881 Patterns in a Visuomotor Behavior Increases Speed. Curr Biol 30:788-801.e3.
882 Jonaitis J. 2020. Probing the interconnectivity of rhythm generating modules in Drosophila
883 melanogaster larvae. University of St Andrews. doi:10.17630/sta/42
884 Josset N, Roussel M, Lemieux M, Lafrance-Zoubga D, Rastqar A, Bretzner F. 2018. Distinct
885 Contributions of Mesencephalic Locomotor Region Nuclei to Locomotor Control in the Freely
886 Behaving Mouse. Curr Biol 28:884-901.e3.
887 Kiehn O. 2016. Decoding the organization of spinal circuits that control locomotion. Nat Rev
888 Neurosci 17:224–238.
889 Kilbourne BM. 2013. On birds: scale effects in the neognath hindlimb and differences in the
890 gross morphology of wings and hindlimbs. Biol J Linn Soc Lond.
891 Kilbourne BM, Hoffman LC. 2015. Energetic benefits and adaptations in mammalian limbs:
892 Scale effects and selective pressures. Evolution 69:1546–1559.
893 Kilbourne BM, Hoffman LC. 2013. Scale effects between body size and limb design in

894 quadrupedal mammals. PLoS One 8:e78392.

895 Kohsaka H, Takasu E, Morimoto T, Nose A. 2014. A group of segmental premotor
896 interneurons regulates the speed of axial locomotion in Drosophila larvae. Curr Biol 24:2632–
897 2642.

898 Kohsaka H, Zwart MF, Fushiki A, Fetter RD, Truman JW, Cardona A, Nose A. 2019.
899 Regulation of forward and backward locomotion through intersegmental feedback circuits in
900 Drosophila larvae. Nat Commun 10:2654.

901 Landgraf M, Sánchez-Soriano N, Technau GM, Urban J, Prokop A. 2003. Charting the
902 Drosophila neuropile: a strategy for the standardised characterisation of genetically
903 amenable neurites. Dev Biol 260:207–225.

904 Lemon WC, Pulver SR, Höckendorf B, McDole K, Branson K, Freeman J, Keller PJ. 2015.
905 Whole-central nervous system functional imaging in larval Drosophila. Nat Commun 6:1–16.

906 Li H-H, Kroll JR, Lennox SM, Ogundeyi O, Jeter J, Depasquale G, Truman JW. 2014. A GAL4
907 driver resource for developmental and behavioral studies on the larval CNS of Drosophila.
908 Cell Rep 8:897–908.

909 Marder E, Bucher D. 2001. Central pattern generators and the control of rhythmic movements.
910 Curr Biol 11:R986-96.

911 Mathis A, Mamidanna P, Cury KM, Abe T, Murthy VN, Mathis MW, Bethge M. 2018.
912 DeepLabCut: markerless pose estimation of user-defined body parts with deep learning. Nat
913 Neurosci 21:1281–1289.

914 Matsunaga T, Fushiki A, Nose A, Kohsaka H. 2013. Optogenetic perturbation of neural
915 activity with laser illumination in semi-intact drosophila larvae in motion. J Vis Exp e50513.

916 Melcher C, Pankratz MJ. 2005. Candidate gustatory interneurons modulating feeding
917 behavior in the Drosophila brain. PLoS Biol 3:e305.

918 Minassian K, Hofstoetter US, Dzeladini F, Guertin PA, Ijspeert A. 2017. The Human Central
919 Pattern Generator for Locomotion: Does It Exist and Contribute to Walking? Neuroscientist
920 23:649–663.

921 Nirody JA, Duran LA, Johnston D, Cohen DJ. 2021. Tardigrades exhibit robust interlimb
922 coordination across walking speeds and terrains. Proc Natl Acad Sci U S A 118.
923 doi:10.1073/pnas.2107289118
924 Ohyama T, Schneider-Mizell CM, Fetter RD, Aleman JV, Franconville R, Rivera-Alba M,
925 Mensh BD, Branson KM, Simpson JH, Truman JW, Cardona A, Zlatic M. 2015. A multilevel
926 multimodal circuit enhances action selection in Drosophila. Nature 520:633–639.
927 Pfeiffer BD, Ngo T-TB, Hibbard KL, Murphy C, Jenett A, Truman JW, Rubin GM. 2010.
928 Refinement of tools for targeted gene expression in Drosophila. Genetics 186:735–755.
929 Pfeiffer BD, Truman JW, Rubin GM. 2012. Using translational enhancers to increase
930 transgene expression in Drosophila. Proc Natl Acad Sci U S A 109:6626–6631.
931 Picao-Osorio J, Johnston J, Landgraf M, Berni J, Alonso CR. 2015. MicroRNA-encoded
932 behavior in Drosophila. Science 350:815–820.
933 Pratt CA, Jordan LM. 1987. Ia inhibitory interneurons and Renshaw cells as contributors to
934 the spinal mechanisms of fictive locomotion. J Neurophysiol 57:56–71.
935 Roberts A, Li W-C, Soffe SR. 2010. How neurons generate behavior in a hatchling amphibian
936 tadpole: an outline. Front Behav Neurosci 4:16.
937 Rocha-Barbosa O, De Castro Loguercio MF, Renous S, Gasc J-P. 2005. Limb joints
938 kinematics and their relation to increasing speed in the guinea pig Cavia porcellus
939 (Mammalia: Rodentia). J Zool 266:293–305.
940 Ryczko D, Grätsch S, Schläger L, Keuyalian A, Boukhatem Z, Garcia C, Auclair F, Büschges
941 A, Dubuc R. 2017. Nigral Glutamatergic Neurons Control the Speed of Locomotion. J
942 Neurosci 37:9759–9770.
943 Saalfeld S, Cardona A, Hartenstein V, Tomancak P. 2009. CATMAID: collaborative
944 annotation toolkit for massive amounts of image data. Bioinformatics 25:1984–1986.
945 Santos JG, Vömel M, Struck R, Homberg U, Nässel DR, Wegener C. 2007.
946 Neuroarchitecture of peptidergic systems in the larval ventral ganglion of Drosophila
947 melanogaster. PLoS One 2:e695.

948 Saravanan V, Berman GJ, Sober SJ. 2020. Application of the hierarchical bootstrap to multi-
949 level data in neuroscience. Neuron Behav Data Anal Theory 3.
950 Schnorrer F, Kalchhauser I, Dickson BJ. 2007. The transmembrane protein Kon-tiki couples
951 to Dgrip to mediate myotube targeting in Drosophila. Dev Cell 12:751–766.
952 Schultheis D, Weißkopf M, Schaub C, Ansari S, Dao VA, Grossmann D, Majumdar U,
953 Hakeemi MS, Troelenberg N, Richter T, Schmitt-Engel C, Schwirz J, Ströhlein N, Teuscher
954 M, Bucher G, Frasch M. 2019. A Large Scale Systemic RNAi Screen in the Red Flour Beetle
955 Tribolium castaneum Identifies Novel Genes Involved in Insect Muscle Development. G3
956 9:1009–1026.
957 Schützler N, Girwert C, Hügli I, Mohana G, Roignant J-Y, Ryglewski S, Duch C. 2019.
958 Tyramine action on motoneuron excitability and adaptable tyramine/octopamine ratios adjust
959 Drosophila locomotion to nutritional state. Proc Natl Acad Sci U S A 116:3805–3810.
960 Shik ML, Orlovsky GN. 1976. Neurophysiology of locomotor automatism. Physiol Rev
961 56:465–501.
962 Shik ML, Severin FV, Orlovskiĭ GN. 1966. [Control of walking and running by means of
963 electric stimulation of the midbrain]. Biofizika 11:659–666.
964 Skinner RD, Garcia-Rill E. 1984. The mesencephalic locomotor region (MLR) in the rat. Brain
965 Res 323:385–389.
966 Song J, Pallucchi I, Ausborn J, Ampatzis K, Bertuzzi M, Fontanel P, Picton LD, El Manira A.
967 2020. Multiple Rhythm-Generating Circuits Act in Tandem with Pacemaker Properties to
968 Control the Start and Speed of Locomotion. Neuron 105:1048-1061.e4.
969 Sun X, Liu Y, Liu C, Mayumi K, Ito K, Nose A, Kohsaka H. 2022. A neuromechanical model
970 for Drosophila larval crawling based on physical measurements. BMC Biol 20:130.
971 Takagi S, Cocanougher BT, Niki S, Miyamoto D, Kohsaka H, Kazama H, Fetter RD, Truman
972 JW, Zlatic M, Cardona A, Nose A. 2017. Divergent Connectivity of Homologous Command-
973 like Neurons Mediates Segment-Specific Touch Responses in Drosophila. Neuron 96:1373-
974 1387.e6.

975 Talay M, Richman EB, Snell NJ, Hartmann GG, Fisher JD, Sorkaç A, Santoyo JF, Chou-
976 Freed C, Nair N, Johnson M, Szymanski JR, Barnea G. 2017. Transsynaptic Mapping of
977 Second-Order Taste Neurons in Flies by trans-Tango. Neuron 96:783-795.e4.
978 Trimmer B, Issberner J. 2007. Kinematics of soft-bodied, legged locomotion in Manduca
979 sexta larvae. Biol Bull 212:130–142.
980 Zarin AA, Mark B, Cardona A, Litwin-Kumar A, Doe CQ. 2019. A multilayer circuit architecture
981 for the generation of distinct locomotor behaviors in Drosophila. Elife 8.
982 doi:10.7554/eLife.51781
983 Zwart MF, Pulver SR, Truman JW, Fushiki A, Fetter RD, Cardona A, Landgraf M. 2016.
984 Selective Inhibition Mediates the Sequential Recruitment of Motor Pools. Neuron
985
986 **Table 1. Key resources**
987

Reagent type	Designation	Source or reference	Additional information
Fly strain	yw	BDSC #6598	
	GMR24H08-GAL4.AD	BDSC #68300	
	GMR45F08-GAL4.DBD	BDSC #70239	
	GMR44F09-GAL4.DBD	BDSC #71061	
	GMR41F02-GAL4.AD	BDSC #75660	
	R76E09-LexA	BDSC #54951	A26f-LexA

	VT050223-GAL4.AD	BDSC #72931	
	R15E05-GAL4.DBD	BDSC #68731	
	GMR45F08-GAL4	BDSC #49565	A31c-a8-Gal4
	GMR76E09-GAL4	BDSC #39931	A26f-GAL4
	GMR41F02-LexA	BDSC #54794	A31c-LexA
	nSyb-LexA_VK00027	This study	
	eve[RRa-F]-GAL4	gift from Dr. Miki Fujioka	
	sr-GAL4	BDSC #26663	
	UAS-CD4::GCaMP6f_atp40	(Kohsaka et al., 2014)	
	LexAop2-RGECO1_VK00005	(Kohsaka et al., 2014)	
	LexAop-jRCaMP1b	BDSC #64428	
	20XUAS-6XGFP	BDSC #52262	
	trans-Tango	BDSC #77124	
	MCFO-4	BDSC #64088	

	mhc-GFP	gift from Dr. Cynthia L. Hughes	
	UAS-CsChrimson::mVenus	BDSC #55136	
	UAS-GtACR1_attp2	gift from Dr. Chris Doe	
	UAS-VNC-CsChrimson	gift from Dr. Karen Hibbard (Hiramoto et al., 2021)	
Antibody	rabbit anti-GFP	Af2020, Frontier Institute	1:1000
	mouse anti-FAS2	1D4, DSHB	1:10
	guinea pig anti-GFP	Af1180, Frontier Institute	1:1000
	rabbit anti-HA	C29F4, Cell Signaling Technology	1:1000
	mouse anti-ChAT	4B1, DSHB	1:50
	rabbit anti-GABA	A2052, Sigma;	1:100
	mouse anti-VGluT	Gift from Dr. Hermann Aberle	1:1000
	rabbit anti-DsRed	#632496, Clontech	1:500
	goat Alexa Fluor	A-11034,	1:300

	488-conjugated anti-rabbit IgG	Invitrogen Molecular Probes	
	goat Alexa Fluor 555-conjugated anti-mouse IgG	A-21424, Invitrogen Molecular Probes	1:300
	goat Alexa Fluor 488-conjugated anti-guinea pig IgG	A-11073, Invitrogen Molecular Probes	1:300

988

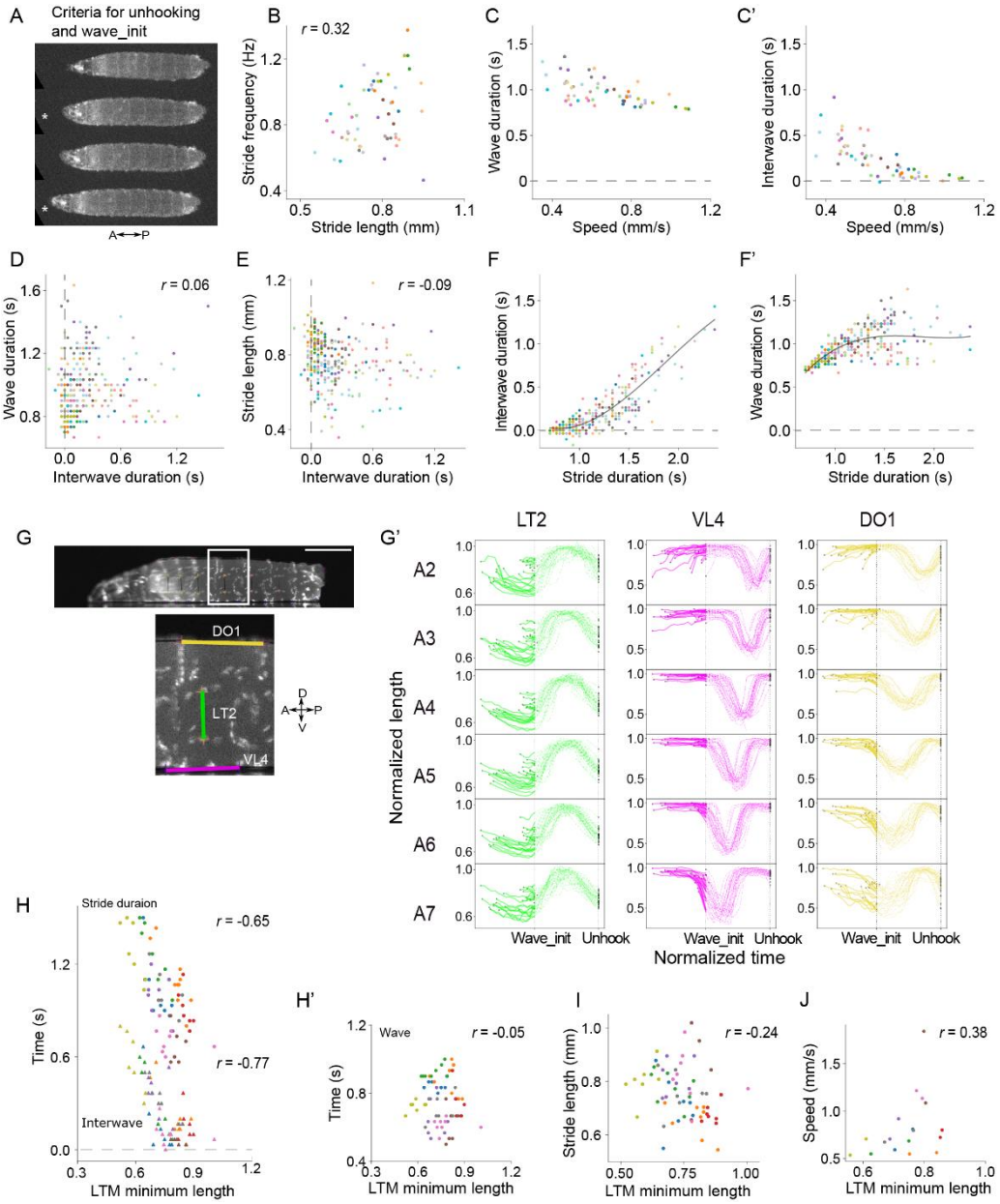

Figure 1 - supplement

(A-F) Supplement to top-view crawling assay. **(A)** Criteria to determine the unhooking moment and the wave initiation moment (See Materials and methods for details.) Asterisks indicate the key frames (upper asterisk: unhooking moment; lower asterisk: wave initiation moment). **(B)** Relationship between stride frequency and stride length. **(C-C')** Relationship between speed and the two component phases (Pearson correlation coefficient: -0.74 for interwave phase and -0.62 for the wave duration; p-value = 0.127). **(D)** Relationship between the duration of wave phase and interwave phase. **(E)** Relationship between stride

998 length and the duration of interwave phase. **(F)** Relationship between stride duration and
999 the duration of component phases. Lines: cubic regression (regression coefficients:
1000 interwave, [0.78, -2.1, 1.7, 0.3]; wave, [0.78, 3.1, -1.7, -0.3]; See Materials and methods for
1001 details.) **(G-J)** Supplement to side-view crawling assay. **(G)** An example frame of side-view
1002 recording. Scale bar: 1 mm. Lower panel is an enlarged image of the region indicated by
1003 the white rectangular in the top panel. The range of muscles (DO1, LT2, and VL4) is
1004 labeled. **(G')** Dynamics of muscle length during forward crawling measured from the side-
1005 view assay. Muscle length is normalized to 0-1 by 0 and the maximum length of the
1006 muscle. Time is aligned by the wave_init moment and the unhooking moment (See
1007 Materials and methods for details). Each trace initiates and ends at the beginning and end
1008 of a locomotor cycle.
1009

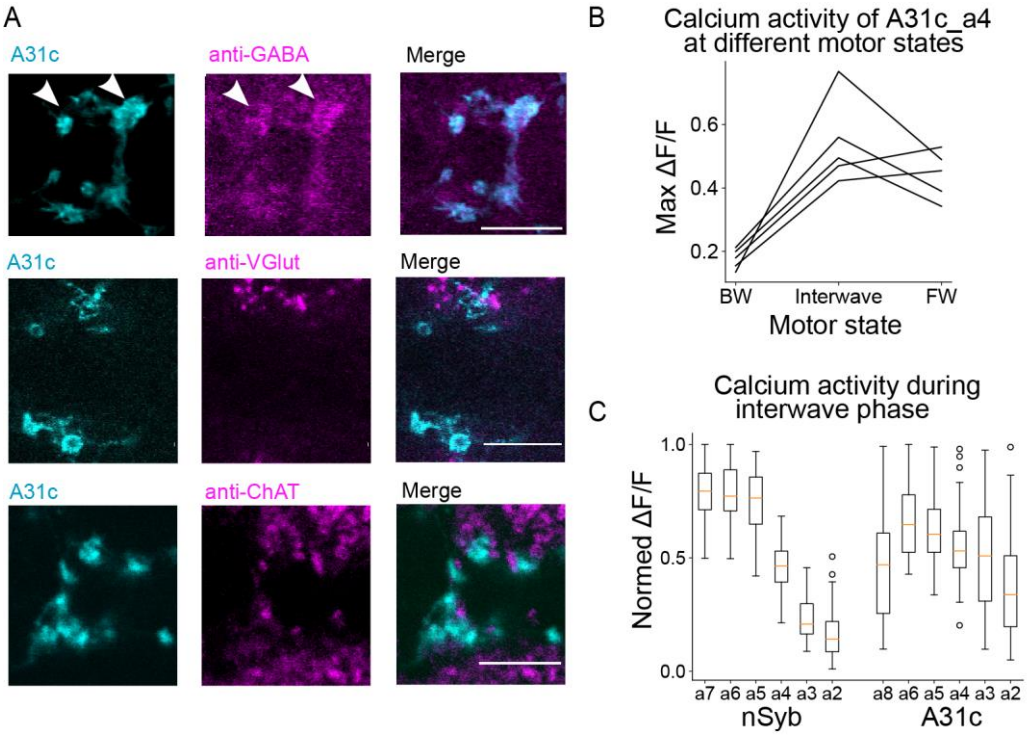

Figure 2-supplement

(A) Immunostaining reveals that A31c neuron is GABAergic. Scale bars: 10 μm. **(B)** Comparison of the amplitude of the peak calcium signals of the A31c_a4 neuron in different motor states (BW: backward wave; PSync: posterior synchronous burst; FW: forward wave). **(C)** Comparison of the amplitude of the peak calcium signals of nSyb neurons and A31c neurons when nSyb-a7 reaches the peak (See magenta arrowheads in Figure 2E.)

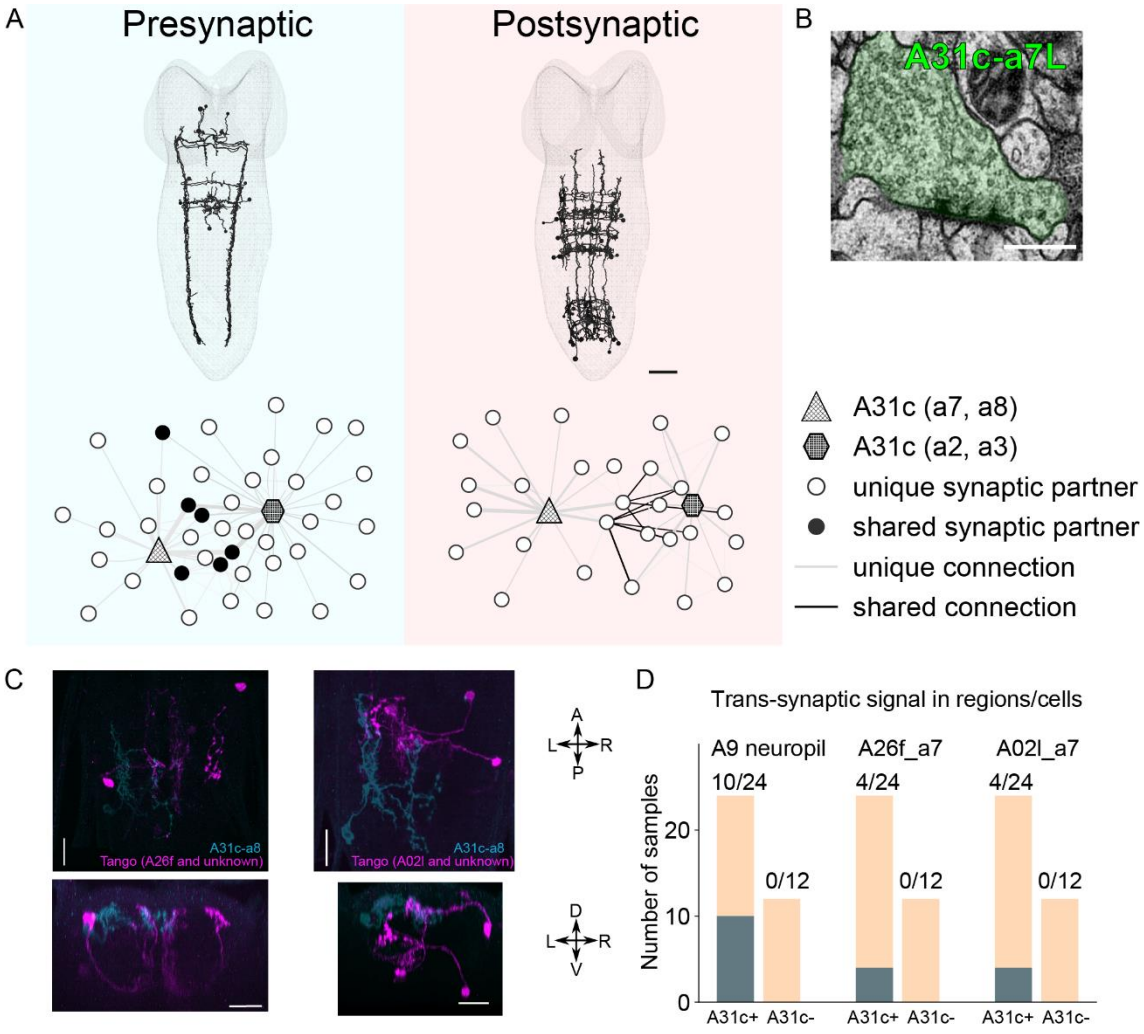

Figure 3-supplement

(A) Reconstructed main synaptic partners of A31c neurons. **(B)** A sample EM image shows the A31c presynaptic site. **(C)** *trans*-Tango reveals the postsynaptic partners (magenta) of A31c neurons (cyan) (*A31c-a8-sp>trans-Tango*). **(D)** Quantification of the number of samples that shows expression in regions or neurons repeatedly targeted by *trans*-Tango. Scale bars: 20 μm.

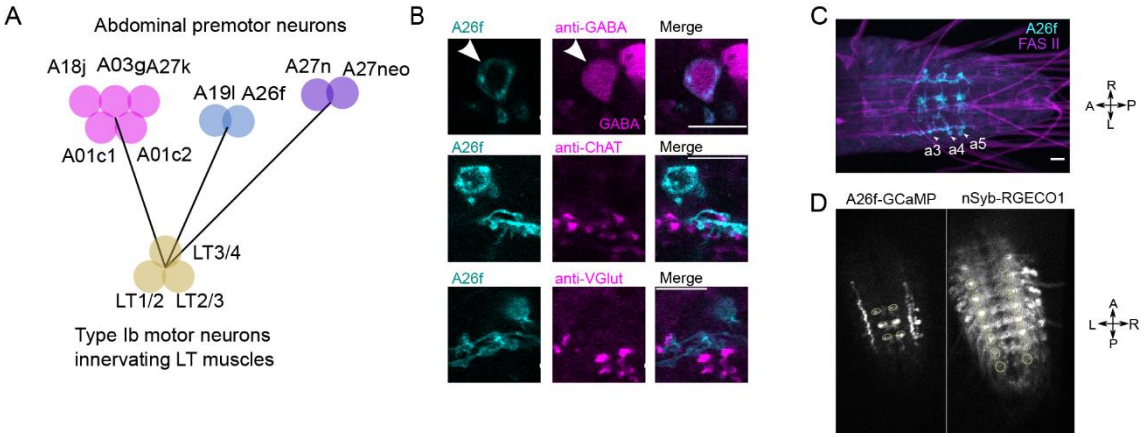

Figure 4-supplement

(A) Premotor interneurons that target all the motor neurons innervating LT muscles. **(B)** Immunostaining reveals that A26f neuron is GABAergic. Scale bars: 10 μm. **(C)** *A26f-sp* labels A26f neurons in A3 to A5 neuromeres. **(D)** Calcium signals of A26f neurons and nSyb neurons in fictive locomotor cycles.

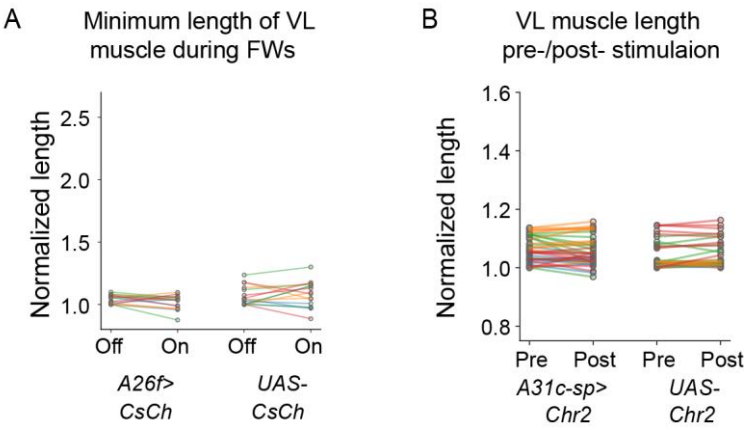

1033

1034 **Figure 5-supplement**

1035 **(A)** The minimum length of longitudinal VL muscles was not affected by optogenetic

1036 activation of A26f neurons. **(B)** The length of VL muscles in the resting state was not

1037 affected by optogenetic activation of A31c neurons.

1038

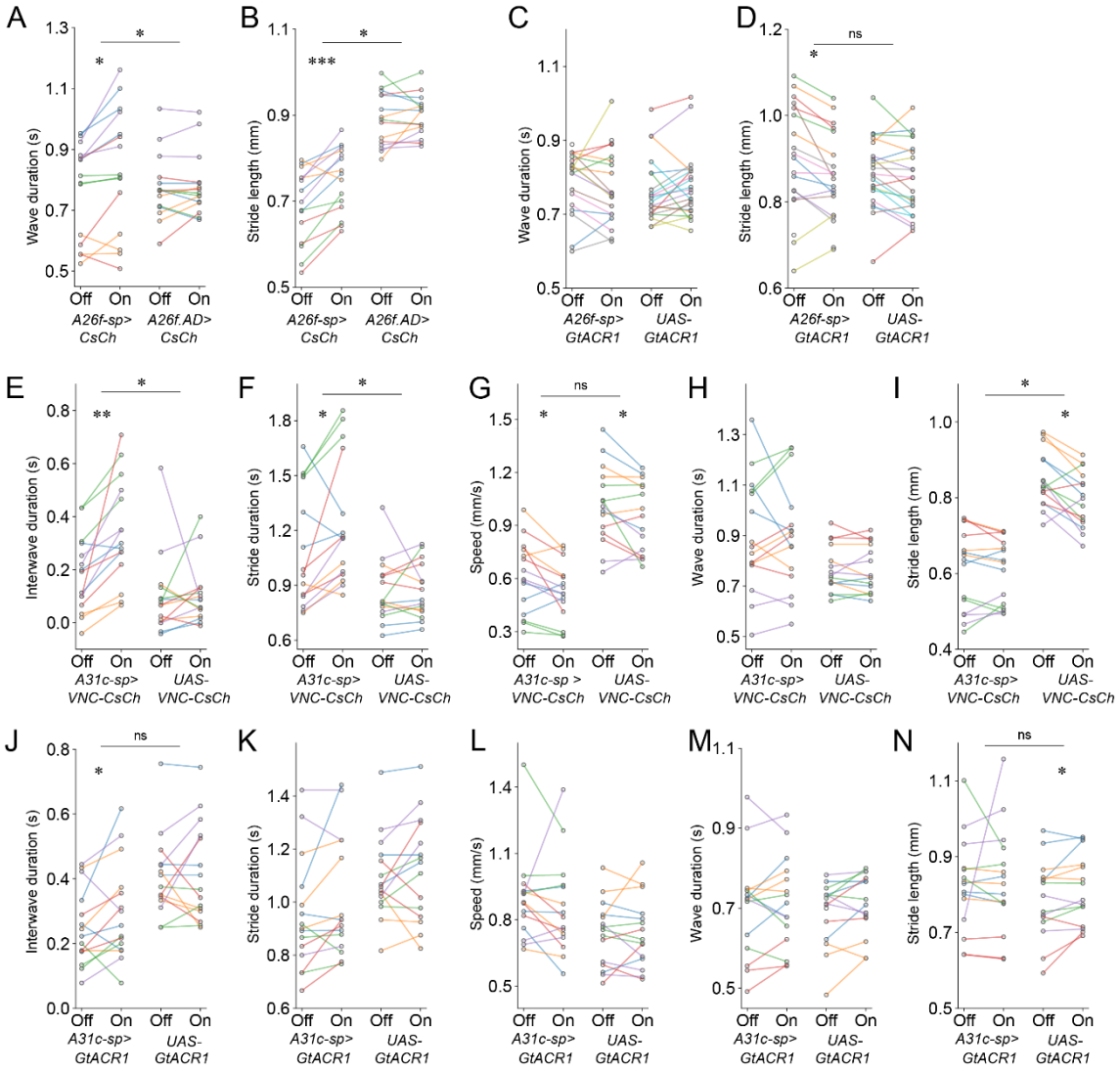

Figure 7-supplement

Analysis of crawling kinematics of larvae with optogenetic perturbation. **(A and B)** Activation of A26f neurons. **(C and D)** Inhibition of A26f neurons. **(E-I)** Activation of A31c neurons. **(J-N)** Inhibition of A31c neurons. Statistical results are obtained by the hierarchical bootstrap test (See Materials and methods for details.)